Behaviour of structural engineered cementitious composites under dynamic tensile loading and elevated temperatures

Meng Chen [a,b], Yuting Wang [a], Tong Zhang [a,c], Mingzhong Zhang [c,*]

[a] School of Resources and Civil Engineering, Northeastern University, Shenyang 110819, China

[b] Institute for Frontier Technologies of Low-Carbon Steelmaking, Northeastern University, Shenyang 110819, China

[c] Department of Civil, Environmental and Geomatic Engineering, University College London, London WC1E 6BT, United Kingdom

Abstract: This paper presents a systematic study on dynamic splitting tensile properties of polyvinyl alcohol (PVA) fibre reinforced engineered cementitious composites (ECC) after exposure to elevated temperatures up to 800 °C under strain rates of 4.34 to 10.95 s^{-1}. A series of tests were conducted to characterise the weight loss, elastic modulus, uniaxial tensile properties, static and dynamic splitting tensile behaviour, and pore pressure, as well as the chemical and microstructural evolution of ECC. Results indicate that the dynamic splitting tensile properties of ECC went up with the increasing strain rate regardless of heated temperatures due to strain rate effect. The dynamic splitting strength, dynamic increase factor and energy dissipation of ECC reached the maximum values at 105 °C, which can be ascribed to the enhanced fibre-matrix bond and further hydration of fly ash. However, the dynamic tensile properties of ECC reduced at over 250 °C due to the melting of PVA fibres, thermally induced microcracks and dehydration of hydration products. At 800 °C, the dynamic splitting tensile strength and dissipated energy of ECC dropped by 81.0–83.2% and 88.4–89.1% over the measured strain rate range, relative to that at 20 °C. In addition, the main role for resisting dynamic loading was gradually transferred from fibre debonding-elongating action to crack propagation at over 400 °C. Accordingly, the failure patterns of ECC changed from tensile failure with the main central crack to coupled tensile-shear failure with multiple cracks.

Keywords: Fibre reinforced concrete; Strain-hardening cementitious composites; Tensile behaviour; Dynamic properties; Thermal resistance; Microstructure

1. Introduction

In service, the concrete infrastructures may be exposed to extreme conditions such as earthquakes, explosions, fires and other types of eventualities [1]. For instance, in 2014, a crash involving two trucks transporting hazardous chemicals in the Yanhou tunnel, China, resulting in the death of over 30 people and the burning of 1500 tonnes of coal [2]. The explosion caused by the burning process

---

* Corresponding author. E-mail address: mingzhong.zhang@ucl.ac.uk (M. Zhang)

led to serious damage to the tunnel lining. To improve the impact resistance of structural materials, engineered cementitious composites (ECC) have been designed and regarded as a special class of high-performance fibre reinforced cementitious composites [3,4]. Compared to ordinary concrete or fibre reinforced concrete, ECC has unique characteristics including strain-hardening behaviour with an ultimate tensile strain capacity of over 3% as well as multiple microcracking with an average crack width of no more than 60 μm [5]. Synthetic polymer fibres including polyvinyl alcohol (PVA) and polyethene (PE) fibres are widely adopted to reinforce the ECC matrix [6,7]. Moreover, ECC has self-healing capability, superior durability, and high resistance to shrinkage, impact and fire attacks [8–12]. Thus, ECC has attracted a lot of interests with widespread structural applications such as structural elements, tunnel lining strengthening, surface coatings, dam installation, bridge deck paving, paving connection, coupling beams installation and so on [13–17].

Recently, an increasing number of attentions have been paid to ECC, with particular interests in the evolution of mechanical properties, phase composition and microstructural characteristics at elevated temperatures. When exposed to a temperature below 200 °C, the mechanical properties of ECC are probably enhanced with the increase of fly ash content [1,18–20], while its compressive strength significantly drops with the increasing temperature above 200 °C [21]. The residual compressive strength of PVA fibre reinforced ECC (by retaining 53% of its original compressive strength after 600 °C) [22] was found to be similar to or even greater than that of polypropylene fibre reinforced concrete (50% remained after 600 °C) [23] or steel fibre reinforced concrete (39% remained after 600 °C) [24]. After being exposed to 800 °C, the residual compressive strength of ECC is only about 20–51% of that at room temperature [9,15,19,25]. In terms of tensile properties of ECC, when the temperature reaches the melting point of polymer fibres, the tensile strength of fibres drops significantly and the strain-hardening and multiple cracking characteristics of ECC gradually diminish [20,26,27]. Although the continuous hydration of cement and the pozzolanic reaction of fly ash may lead to an increase in tensile strength at over 200 °C [18,20,28,29], the decomposition of cement hydrates had an adverse effect on tensile properties at higher temperatures [21,30,31]. Apart from the melting of polymer fibres, the microcracks caused by thermal stress and growing porosity would inevitably lead to the strength loss of ECC [32]. So far, the mechanical properties of ECC at elevated temperatures have been extensively studied, while the microstructure-tensile behaviour relationships in ECC at various temperatures have been rarely explored.

To date, several attempts have been made to investigate the dynamic behaviour of ECC, including dynamic compressive properties [33,34], dynamic tensile properties [35,36] and dynamic spalling properties [37]. Under the split Hopkinson pressure bar (SHPB) test, the compressive strength and

ultimate strain of ECC went up by 27–31% and 42–52%, respectively, with the increase of strain rate from 96 to 197 s^{-1}, implying a strong strain rate dependence [33]. The incorporation of 2.0 vol% PVA fibre into ECC resulted in a 60–70% rise in compressive ductility and superior energy absorption capacity [34]. An experimental study on the dynamic tensile behaviour of PVA fibre reinforced ECC indicated that the tensile strength and strain capacity raised by 53% and 163%, respectively, as the strain rate increased from 10 to 50 s^{-1} [36]. The enhanced bond between fibres and the ECC matrix was the main factor that improved the tensile strength and ductility of ECC with the increasing strain rate [35]. Additionally, the dynamic spalling tests on ECC within the strain rate range of 140–180 s^{-1} also suggested that PVA fibre reinforced ECC exhibited higher fracture energy and a more significant strain rate effect, as compared to high-strength concrete and ultra-high performance concrete. This can be ascribed to the generation of multiple microcracks and the bridging effect of fibres in ECC [37]. However, the splitting tensile properties of ECC under dynamic loadings are rarely studied, and the coupled effect of strain rate and elevated temperatures on the dynamic tensile performance of ECC has not been explored yet, which would hinder the potential applications of ECC structural elements in dynamic/thermal environment.

Compared to the melting point of PE fibre at around 120 °C, PVA fibre has a higher melting point (around 250 °C) and could delay the deterioration of ECC at elevated temperatures [27,38]. With this consideration, the main purpose of this study is to gain a comprehensive understanding of the static and dynamic tensile properties of PVA fibre reinforced ECC after exposure to different temperatures (20, 105, 250, 400, 600 and 800 °C) under various strain rates (4.34–10.95 s^{-1}). A series of tests were conducted to measure the physical and mechanical properties of ECC at elevated temperatures including weight loss, elastic modulus, uniaxial tensile behaviour, static and dynamic splitting tensile properties, and pore pressure. The thermal performance and microstructural evolution of ECC were characterised by thermal analysis, X-ray diffractometer (XRD), scanning electron microscope (SEM) and mercury intrusion porosimetry (MIP), based on which the evolution of dynamic splitting tensile properties of ECC in relation to its phase stability and microstructural evolution was analysed and the dynamic damage mechanism of ECC subjected to elevated temperatures was systematically discussed.

2. Experimental program

2.1 Raw materials

Ordinary Portland cement (P.I. 42.5R) with specific gravity of 3.09 and low-calcium fly ash were used as binders to produce ECC, the chemical composition of which is presented in Table 1. Silica sand with maximum size of 250 μm and median size of 130 μm was adopted as fine aggregate. The particle size distribution of cement, fly ash and silica sand was in the ranges of 0.5–50 μm, 0.6–80

μm, and 0.6–100 μm, respectively. The polycarboxylate-based superplasticiser (SP) was added to ensure the acceptable workability of ECC.

PVA fibres (Kuraray Co., Ltd., Japan) treated with 1.2 wt% oil coating were used as reinforcement to make ECC. Due to the hydrophilic properties of PVA fibres, the oil treatment can reduce the adhesion between fibres and the ECC matrix. Thus, the fibres would be relatively easier to slip out of the matrix and be pulled out rather than rupture during crack development [7]. The physical and mechanical properties of PVA fibres are summarised in Table 2.

Table 1 Chemical composition (wt%) of cement and fly ash.

Composition	SiO_2	Al_2O_3	Fe_2O_3	CaO	K_2O	TiO_2	MgO	SO_3	MnO	Na_2O	LOI
Cement	19.39	4.34	3.14	68.07	0.74	0.21	1.37	2.40	0.04	0.01	2.40
Fly ash	56.95	32.40	3.09	2.91	2.08	1.25	0.52	0.36	0.07	0.03	2.45

Note: LOI (Loss on Ignition).

Table 2 Properties of PVA fibre.

Length (mm)	Diameter (μm)	Density (kg/m³)	Melting point (°C)	Vaporisation point (°C)	Tensile strength (MPa)	Elastic modulus (GPa)
12	40	1300	248	439	1560	41

2.2 Mix proportion and sample preparation

The mix proportion of ECC is shown in Table 3, where the water-to-binder ratio is 0.27 and the weight ratio of cement, fly ash and silica sand was 1: 1.2: 0.8. The dosage of SP was 0.4% of cementitious binders. The volume fraction of PVA fibre was set as 2.0%. Regarding the mixing procedure, the dry ingredients including cement, fly ash and silica sand were first mixed for 2 min to guarantee homogeneous dispersion. Then, water was added to the mixture, followed by mixing for another 5 min. After that, SP was added to the mixture and mixed for another 4 min. Finally, PVA fibres were gradually added for 3 min to ensure the even dispersion of fibres The mixture was poured into plastic moulds with various dimensions. All specimens were demoulded after 24 h and then cured in a standard curing room (20 ± 2 °C and 95% relative humidity) until the testing age.

Table 3 Mix proportion of ECC (kg/m³).

Cement	Fly ash	Silica sand	Water	SP	PVA fibre
563	676	451	335	4.98	26

2.3 Heating method

As per ASTM E831 [39], the heating rate was set as 10 °C/min to achieve the five target temperatures, i.e., 105, 250, 400, 600 and 800 °C. After achieving each target temperature, ECC specimens were kept at that temperature for 2 h to ensure a stable thermal state and uniform temperature distribution inside the specimens, and then naturally cooled down after the high-temperature furnace was switched

off.

2.4 Testing methods

2.4.1 Weight loss test

The weight loss of 50 mm ECC cubes was determined according to the proportion of the weight difference before and after heating to the initial weight, and the weight was measured with an accuracy of 0.1 g.

2.4.2 Elastic modulus test

The elastic modulus was measured using three cylindrical ECC specimens (Φ 100 mm×200 mm) at each temperature according to ASTM C469 [40]. 40% of the ultimate load was taken as the target load value under uniaxial compression, and the elastic modulus was calculated as the average slope of stress-strain curves. The loading rate was kept at 1.0 mm/min on all heated specimens.

2.4.3 Uniaxial tensile test

Uniaxial tensile tests were performed on dog-bone-shaped ECC specimens using a universal tensile testing machine with a maximum capacity of 50 kN. The loading rate was 0.5 mm/min as per the recommendation by the Japan Society of Civil Engineers [41]. Fig. 1 illustrates the test set-up and dimensions of the ECC specimen, where two linear variable displacement transducers (LVDTs) were installed on both sides of the specimen to measure the deformation with a length of 80 mm and width of 30 mm. Three specimens were adopted for testing at each temperature and the average value was taken as the uniaxial tensile strength of ECC.
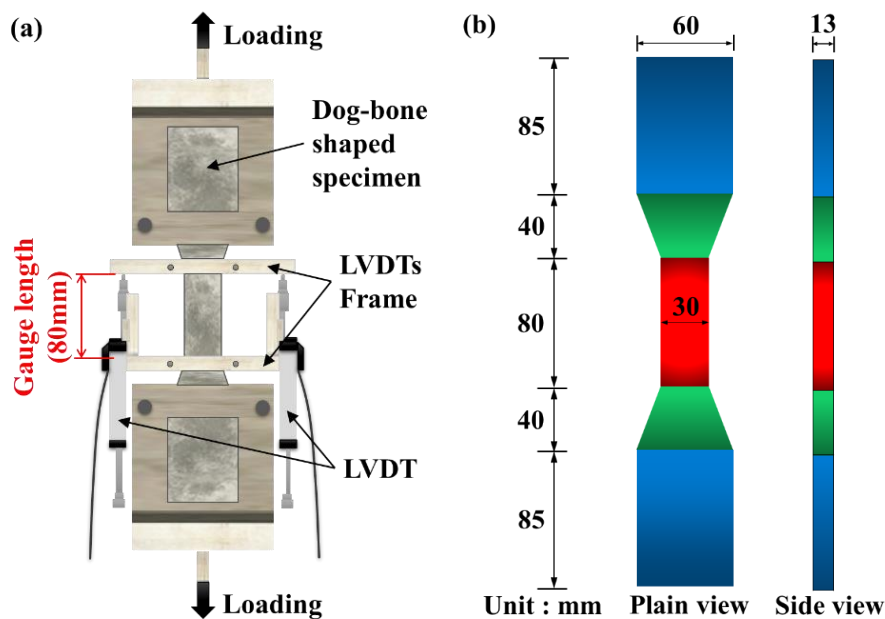

Fig. 1. Uniaxial tensile test: (a) set-up; (b) dimension of the dog-bone shaped specimen.

2.4.4 Static splitting tensile test

The static splitting tensile tests were conducted on ECC specimens (Φ 100 mm×50 mm). The static

splitting strength (f_s) can be calculated as:

$$f_s = \frac{2F_s}{\pi DB} \qquad (1)$$

where F_s is the maximum load during the testing process (kN), and D and B denote the diameter and length (mm) of the specimen, respectively.

2.4.5 Dynamic splitting tensile test

The dynamic splitting tensile test was performed on ECC specimens with diameter of 100 mm and thickness of 50 mm using a 100 mm diameter SHPB system under various strain rates (10^{-1}–10^{1} s^{-1}), as illustrated in a previous study [42]. When the bullet stroke the incident bar, the stress wave was partly reflected to the incident bar and partly transmitted through the test specimen to the transmission bar after it was transferred to the tested specimen [43]. The dynamic splitting properties of the test specimen can be calculated from the strain in the transmission bar. The splitting tensile stress $F_d(t)$ is described as:

$$F_d(t) = E_0 A_0 \varepsilon_t(t) \qquad (2)$$

where A_0 is the cross-sectional area of the steel bars (mm^2), E_0 denotes the elastic modulus of the steel bars (MPa), and ε_t is the strain of the transmission bar.

The dynamic splitting strength (f_d) can be calculated using Eq. (1) by inputting the change of force provided by Eq. (2). The rate of stress rate ($\dot{\sigma}$) and strain ($\dot{\varepsilon}$) on the tested ECC specimen can be expressed as:

$$\dot{\sigma} = \frac{f_d}{\Box t} \qquad (3)$$

$$\dot{\varepsilon} = \frac{\dot{\sigma}}{E_s} \qquad (4)$$

where $\triangle t$ is the time for the specimen to reach f_d (μs), and E_s is the elastic modulus of ECC (MPa).

2.4.6 Pore pressure test

The pore pressure of ECC specimens (200 mm×200 mm×100 mm) at elevated temperatures was monitored using the test set-up with unilateral heating, as illustrated in a previous study [44], where the specimens were heated with a heating rate of 10 °C/min to 800 °C using the electric heating wires positioned at the one side of tested specimen. The K-type thermocouple with a measured range of 20–1000 °C was fixed on the vapour accumulator, and its bottom ends were embedded 25, 50, and 75 mm away from the heating surface during the casting process. The vapour in the pores passed through the steel tube and the connected PVC hoses were filled with silicone oil. The vapour pressure signal was then transmitted to the pressure collector and converted into a current signal [45]. The

thermocouple and pressure collector were connected to the computer to record temperature and pressure data per 10 seconds.

2.4.7 Thermal analysis

The ECC powder samples with a particle size of smaller than 74 μm and PVA fibre were tested and analysed using a differential thermal analysis system (NETZSCH, Germany). Accurately weighted samples were loaded in a crucible under a continuous nitrogen atmosphere of 20 ml/min and ECC samples were heated from 20 to 800 °C with a constant heating rate of 10 °C/min. The evolution of weight loss with temperature is reflected by thermogravimetric (TG) curves, while differential scanning calorimetry (DSC) curves denote the heat transformation of physicochemical reactions.

2.4.8 X-ray diffractometer (XRD)

XRD analysis was carried out on ECC samples of less than 1000 mm^3 with a smooth surface heated to different temperatures using an X-ray diffractometer, MPDDY2094 (PANalytical, the Netherlands), to identify the phase changes of crystalline materials. The 2θ scanning rate with a step size of 0.02° was 6 °/min and the scope of 2θ was 10–80°.

2.4.9 Scanning electron microscope (SEM)

The microstructural evolution of ECC after being subjected to elevated temperatures was observed by Ultra Plus field emission analysis SEM. The morphology of PVA fibres in the ECC matrix under the uniaxial tensile test and the dynamic splitting tensile test was also examined. Before testing, the samples were cut into standard size and sprayed with gold at ambient temperature. The ideal observation position was marked after it has been found for obtaining the thermal change at a fixed point of the ECC samples. After the first observation, the specimen was heated to the next target temperature and the heating-cooling-observation process was repeated in this way (heating temperature from lower to higher). The imaging was conducted on a flat surface with a length and width of 10–20 mm at an acceleration voltage of 10 kV.

2.4.10 Mercury intrusion porosimetry (MIP)

The evolution in the pore structure of ECC at elevated temperatures was characterised using AutoPore IV 9500 (Mack Corporation, USA). The ECC fragments with a volume of less than 500 mm^3 after exposure to each temperature were selected for MIP tests. The pore size measured was within the range of 0.001–1000 μm.

3. Experimental results

3.1 Weight loss

Fig. 2 shows the weight loss of ECC at various temperatures in comparison with that collected from the literature [15,22,46]. In general, the weight loss of ECC went up with the rising temperature,

mainly attributed to the evaporation of water and phase change of PVA fibre in ECC. Between 20 and 105 °C, the weight loss was 2.83% which can be ascribed to the evaporation of free water in the ECC matrix [15]. When the temperature reached 250 °C, the weight loss significantly increased to 12.4%. At this stage, the free water in ECC evaporated completely whilst part of the C-S-H gels began to decompose releasing bound water. In addition, PVA fibres started to melt at around 248 °C and hence leading to a further drop in weight. At 400 °C, the weight loss of ECC reached 14.0% and the slope of the weight loss curve declined slightly within the temperatures of 250–400 °C, which is consistent with the findings reported in Refs. [15,22,46] that the weight loss of ECC was about 12.3–13.5% at 400 °C. Then, the residual PVA fibres completely evaporated at 400–600°C and dehydration of hydration products continued till 800 °C [47], resulting in a total weight loss of 20.0% at 800 °C.
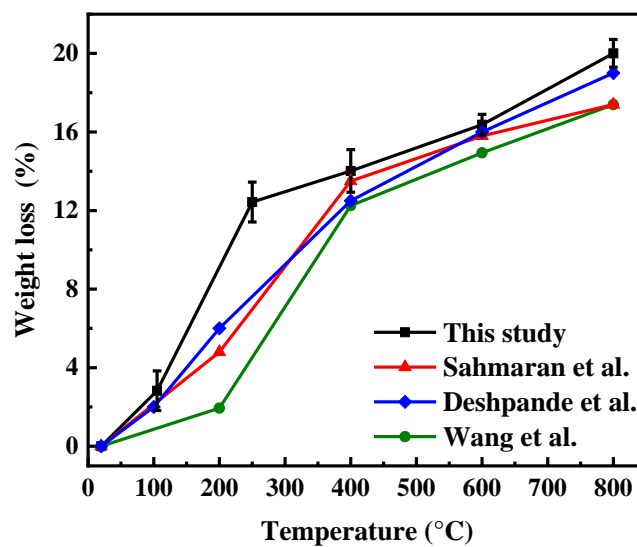

Fig. 2. Weight loss of ECC at elevated temperatures [15,22,46].

3.2 Elastic modulus

Fig. 3 presents the elastic modulus of ECC after being subjected to elevated temperatures. The elastic modulus of ECC was 23.2 GPa at 20 °C, which firstly raised and then declined with the increasing exposure temperature. A slight rise of elastic modulus by 3.2% happened after exposure to 105 °C, indicating the enhancement of deformation capacity [42,48], as the high temperature inside ECC caused by the water evaporation promoted the reaction of fly ash, resulting in a denser microstructure [9,28]. In contrast, the elastic modulus of ECC dropped significantly by 33.6% at 250 °C compared to that at 20 °C. However, after exposure to 400 °C, the elastic modulus of ECC specimens raised again to 18.3 GPa which is 21.1% lower than the initial value. The elastic modulus has a slight rebound at 250–400 °C due to enhanced van der Waal's forces or increased hydration [31,49], but the overall change is not significant. After that, the elastic modulus dropped by 62.5% and 71.6% at 600 °C and 800 °C, respectively, and ECC specimens were damaged rapidly under continuous loading
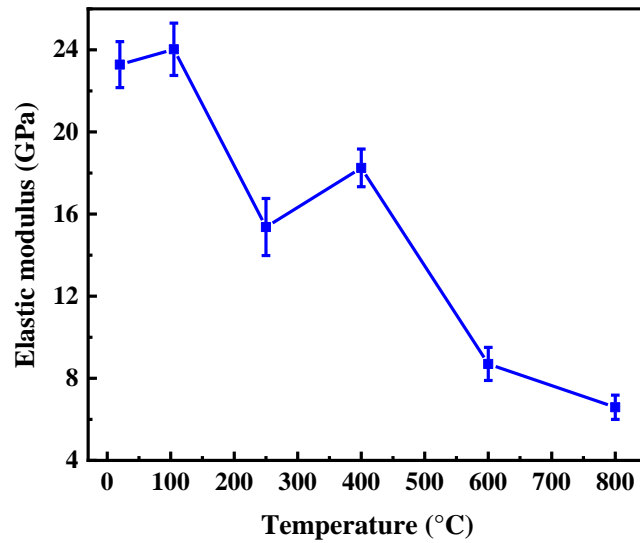
until final failure.

Fig. 3. Elastic modulus of ECC at elevated temperatures.

3.3 Static tensile properties

3.3.1 Uniaxial tensile behaviour

Fig. 4 presents the tensile stress-strain curves of ECC specimens at various temperatures, which can be divided into three regions, including an elastic region, a strain-hardening region, and a failure region. In the elastic region, the tensile stress raised linearly with the increasing tensile strain. The slope of this rising curve represents the tensile elastic modulus of ECC, which dropped with the increasing temperature from 20 °C to 800 °C. The elastic region of tensile stress-strain curves for 20 °C and 105 °C were followed by a fluctuated but gradual increase along with fibre bridging and multiple micro-cracking [50], which led to the desired tensile strain-hardening behaviour and superior ductility [7,51,52]. Moreover, a more obvious strain-hardening region occurred at 105 °C with higher tensile strength and larger ductility. The average tensile strain of ECC was 3.7% at 105 °C and increased by 15.6% compared to that of 20 °C (i.e., 3.2%). A significant drop in tensile stress indicates that dog-bone specimens developed to the failure. When ECC specimens were exposed to 250–800 °C, there was no strain-hardening behaviour and the stress-strain curve only consisted of an elastic region and a sudden failure region. Herein, the elevated temperatures above the melting point of PVA fibre (i.e., 248 °C) had an obvious effect on the deformation capacity of ECC under tension, and the failure pattern changed from ductile failure to brittle failure similar to that of ordinary concrete [20,30].
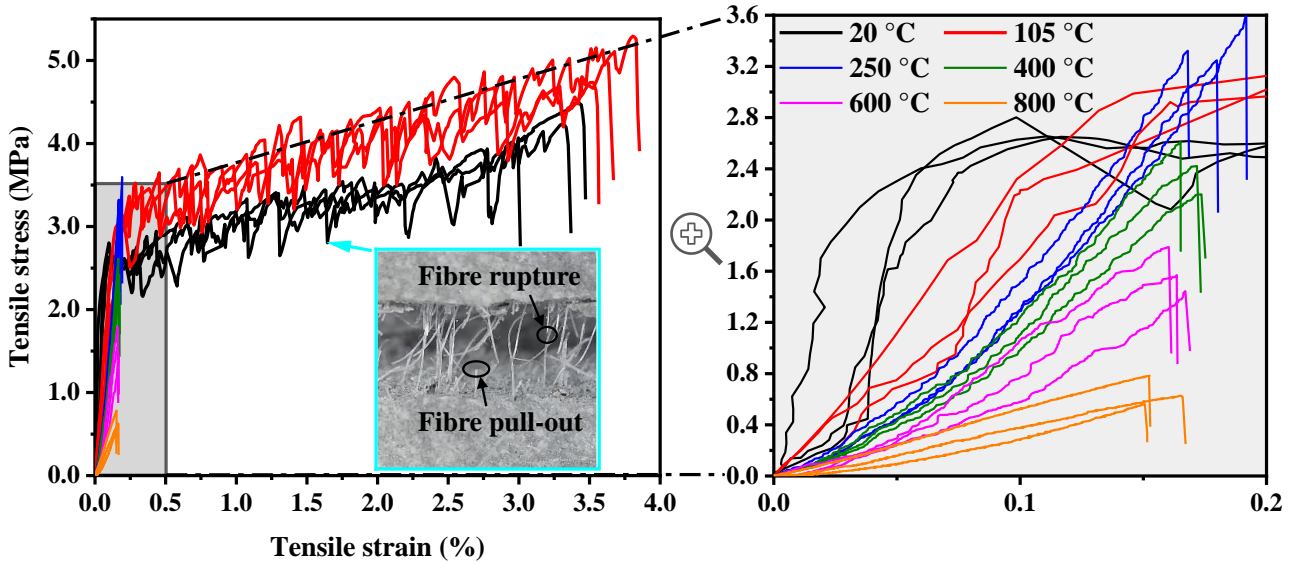
9

Fig. 4. Uniaxial tensile stress-strain curves of ECC at elevated temperatures.

Fig. 5 demonstrates the representative tensile cracking patterns of ECC specimens after being subjected to elevated temperatures. At ambient temperature, multiple microcracks gradually developed on ECC specimens with the increase of tensile load, while PVA fibres bridged the cracks and resisted crack propagation [53]. Besides matrix cracking, the fibre pull-out and rupture can be observed at the crack interface (see Fig. 4). The pull-out end of the fibre is usually smooth and consistent with the initial PVA fibre. When the fibre is elongated until the fracture occurs, its diameter reduces, resulting in a rough and irregular section. PVA fibres played a bridging role before the weakest crack location was changed with the increasing tensile load. However, fibres would be pulled out during the crack development if the next matrix cracking strength was smaller than the fibre tensile strength, while they would be ruptured under tensile load when the next cracking strength exceeded the fibre strength. As seen in Fig. 5a, ECC existed in multiple approximate parallel microcracks and strain-hardening abilities at ambient temperature. At 105 °C, the crack development was more uniform with an increased number of microcracks and reduced crack width, suggesting that the fibre-matrix bond and crack-controlling behaviour were improved [54,55]. With the further increase of exposure temperature to 250 °C, most fibres in the matrix melted with the formation of pores. Thus, the crack formed and expanded rapidly under tensile load until the failure of the specimen [19,56], where only one macroscopic crack appears on the surface of the specimen under tensile load at 250–800 °C.
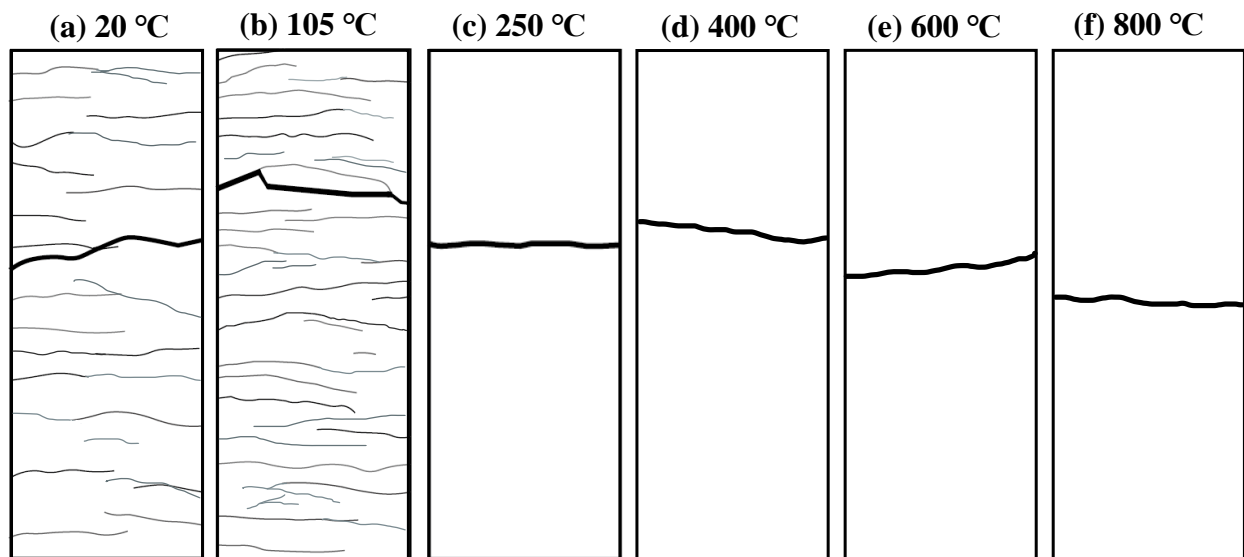
10

Fig. 5. Representative tensile cracking patterns of ECC at elevated temperatures.

Fig. 6 presents the changes in uniaxial tensile strength and first cracking strength of ECC against temperature, in comparison with those obtained from the literature. The tensile strength increased first and then declined with the increase in temperature. After exposure to 105 °C, the uniaxial tensile strength and first cracking strength of ECC went up by about 7.8% and 4.1% compared to that at 20 °C, which is consistent with the previous result that the tensile strength of ECC raised as the temperature increased from 20 to 100 °C [57]. At this stage, the tensile properties of PVA fibres were maintained while the matrix strength was enhanced [20]. Thus, the slight increase in uniaxial tensile strength can be ascribed to the further hydration of ECC binders [19,57,58], which improves the interfacial bond between PVA fibres and matrix as well as fibre bridging action before 200 °C [20,46]. After being exposed to 250, 400, 600, and 800 °C, the uniaxial tensile strength of ECC declined by 24.5%, 46.5%, 66.4%, and 85.3%, respectively, in comparison with that at 20 °C. After fibre melting, the results of available studies show a significant reduction in the uniaxial tensile strength of ECC, as shown in Fig. 6. ECC specimens after being subjected to high temperatures between 250 °C and 800 °C exhibited a brittle tensile failure after initiation of first crack and a sharp drop in uniaxial tensile strength, which can be ascribed to the melting of PVA fibres and damage evolution in ECC matrix [29].
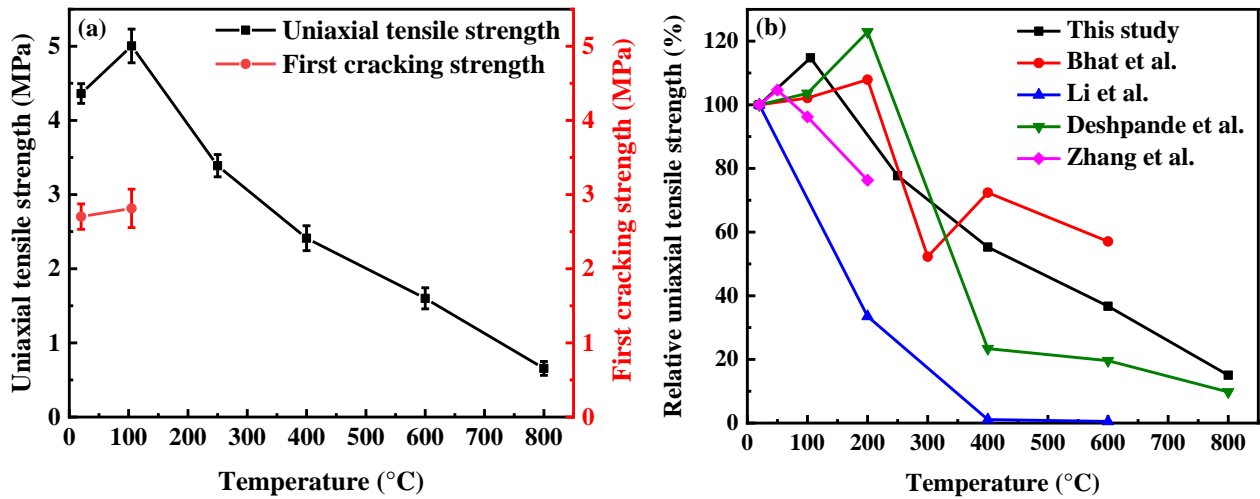
Fig. 6. Uniaxial tensile properties of ECC at elevated temperatures: (a) uniaxial tensile strength and first cracking strength of this study; (b) relative uniaxial tensile strength compared with other studies [19,20,46,58].

3.3.2 Splitting tensile strength

Fig. 7 shows the static splitting tensile strength of ECC at elevated temperatures, indicating that the splitting tensile strength raised at 105 °C and then dropped until 250 °C, followed by a regain at 400 °C and a decline up to 800 °C. The splitting tensile strength of ECC at 20 °C was 9.23 MPa, which was increased by 18.5% after being subjected to 105 °C. It can be ascribed to the compact microstructure and the crack-bridging effect of PVA fibres [9,28,54]. When the temperature reached 250 °C, the splitting tensile strength reduced significantly by 24.7% as PVA fibres started to melt. Then, an obvious increase of 32.5% for splitting tensile strength can be observed at 400 °C, which was still 0.2% lower than the unheated strength. However, the splitting tensile strength of ECC dramatically declined by 51.2% at 600 °C and 78.5% at 800 °C, respectively, compared to that at 20 °C.
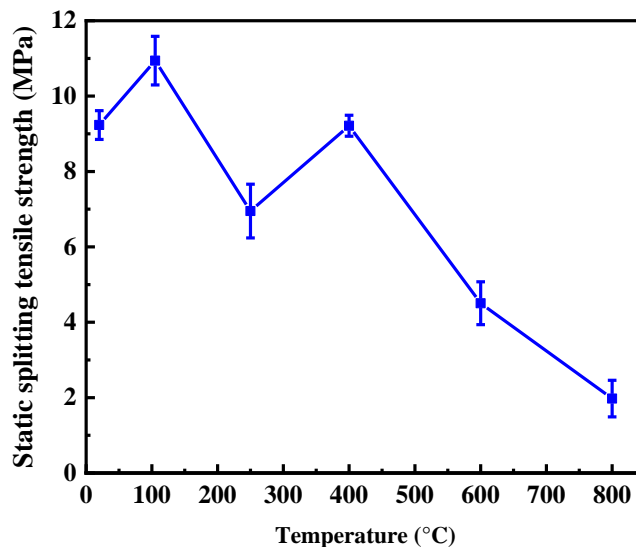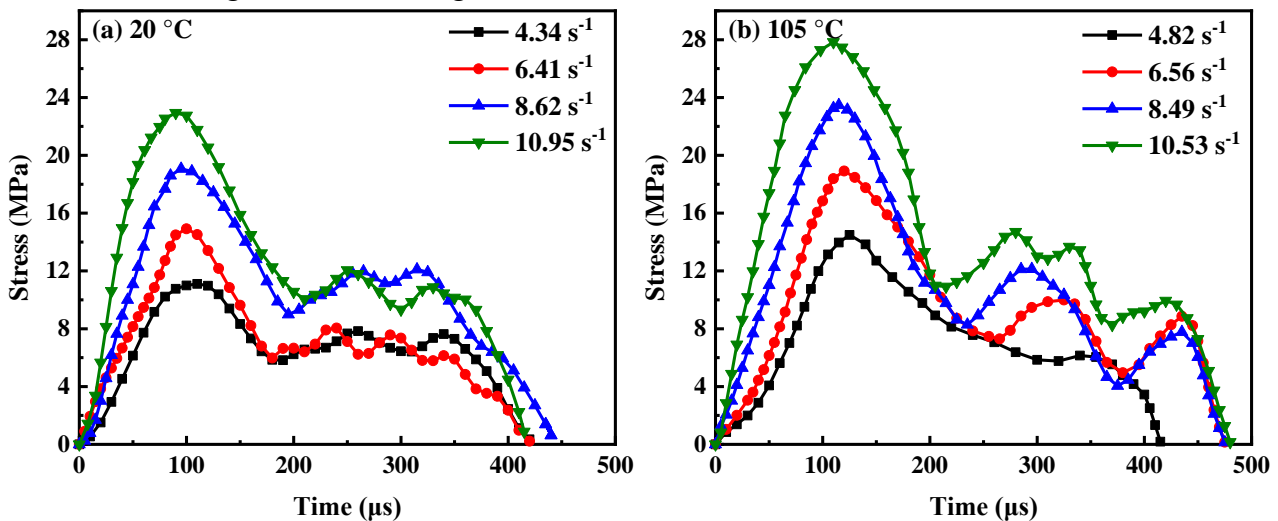

Fig. 7. Static splitting tensile strength of ECC at elevated temperatures.

12

3.4 Dynamic splitting tensile properties

3.4.1 Stress-time response

Various impact velocities were obtained for different air pressures and impact distances, which in turn were applied to calculate the loading strain rate on the test specimen. Then, the strain rate of this research was determined within the range of 4.5–10. 5 s^{-1}. Fig. 8 displays the stress-time curves of ECC at different temperatures under the strain rate range of 4.34–10.95 s^{-1}. The corresponding dynamic splitting tensile properties are listed in Table 4. It can be seen that ECC specimens had a similar change trend of the stress-time curve under dynamic splitting tensile loading, regardless of exposure temperature, which can be divided into three stages, i.e., the ascending stage, the direct descending stage, and the fluctuating descending stage. The curve before reaching the peak stress was the ascending stage of elastic deformation. It is obvious that the time of the ascending stage reduced with the increasing strain rate. After that, ECC specimens entered the direct descending stage, during which the stress gradually dropped with time, showing a typical stress-softening phenomenon. At this stage, the microcracks were gradually generated and extended in ECC specimens. As the load increased, the stress-time curve entered the fluctuating descending stage with multi-peak variation characteristics, especially at 20 °C and 105 °C. Meanwhile, PVA fibres played a bridging role as they were pulled out progressively along with the growth of cracks, causing the fluctuating change in the stress-time curve. The effect of PVA fibres on the dynamic splitting performance of ECC can be mainly reflected by the second and even third peak stress. As the fibres started to melt at over 250 °C, the fluctuating change was significantly reduced (Fig. 8c–f), leaving only two stages of the stress-time curve, i.e., the ascending stage and the direct descending stage. Furthermore, the overall shape of curves tends to be smooth with the increase in temperature, indicating a negative effect on the dynamic splitting performance of ECC. This can be explained by the softening of the ECC matrix and the weakening of the fibre bridge effect.
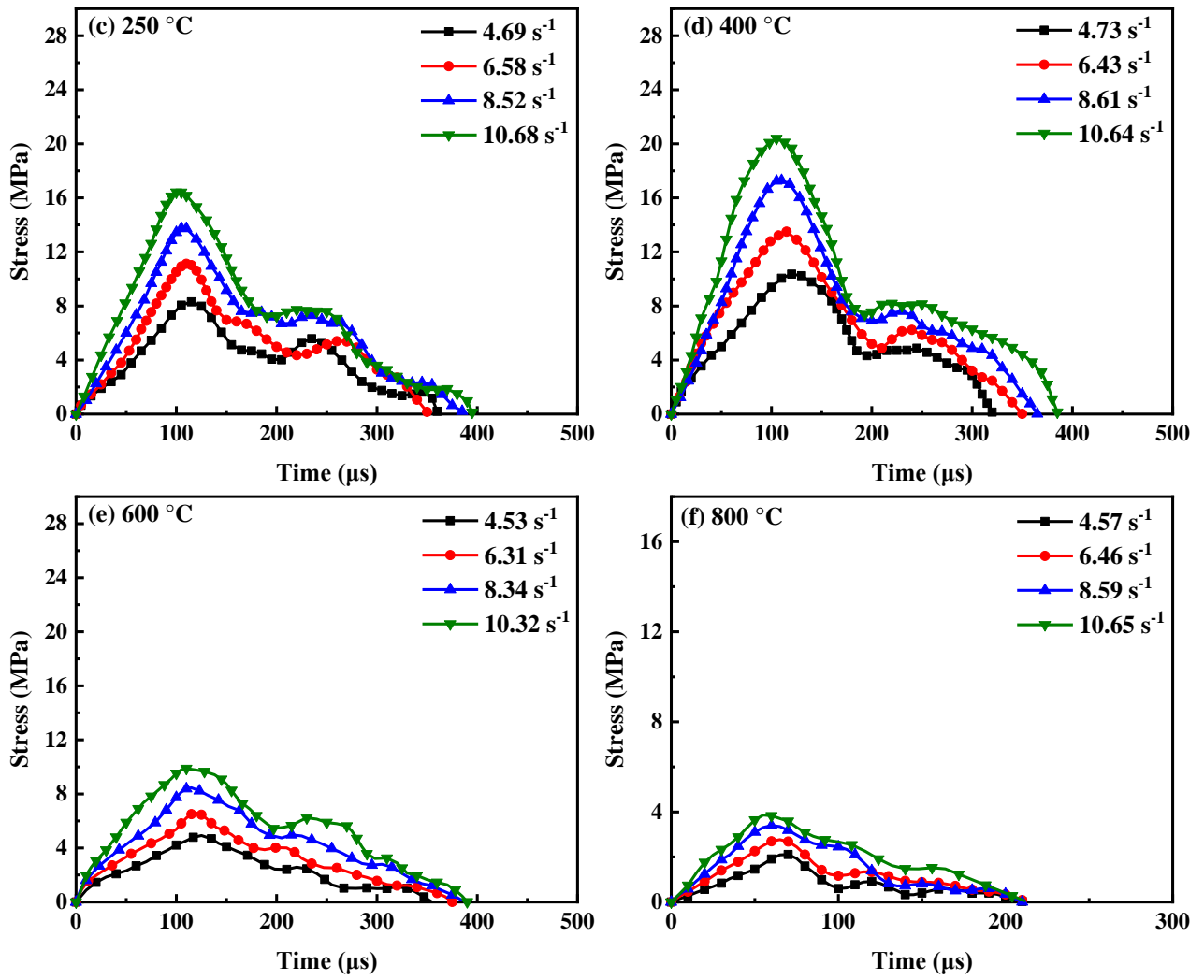
Fig. 8. Representative stress-time curves of ECC at: (a) 20 °C; (b) 105 °C; (c) 250 °C; (d) 400 °C; (e) 600 °C; (f) 800 °C.

Table 4 Summary of static and dynamic properties of ECC at elevated temperatures.

Temperature (°C)	Static splitting tensile strength (MPa)	Average strain rate (s⁻¹)	Dynamic splitting tensile strength (MPa)	DIF	Dissipated energy (J)
20	9.23 ± 0.38	4.34	11.10 ± 0.57	1.20 ± 0.06	86.41 ± 4.53
		6.41	14.92 ± 0.81	1.62 ± 0.09	124.56 ± 6.82
		8.62	19.07 ± 0.98	2.07 ± 0.11	163.48 ± 8.71
		10.95	22.94 ± 1.12	2.49 ± 0.12	201.94 ± 11.07
105	10.94 ± 0.65	4.82	14.49 ± 0.55	1.32 ± 0.05	98.44 ± 6.20
		6.56	18.91 ± 0.38	1.73 ± 0.04	136.19 ± 7.30
		8.49	23.47 ± 0.54	2.15 ± 0.05	177.23 ± 9.50
		10.53	27.83 ± 0.29	2.54 ± 0.03	215.75 ± 15.30
250	6.95 ± 0.71	4.69	8.30 ± 0.26	1.19 ± 0.04	55.83 ± 2.16
		6.58	11.12 ± 0.33	1.60 ± 0.05	77.72 ± 5.76
		8.52	13.75 ± 0.46	1.98 ± 0.07	94.84 ± 12.40
		10.68	16.41 ± 0.32	2.36 ± 0.05	110.62 ± 13.57

14

400	9.21 ± 0.28	4.73	10.36 ± 0.66	1.12 ± 0.07	61.98 ± 2.12
		6.43	13.50 ± 0.41	1.47 ± 0.04	88.13 ± 3.75
		8.61	17.29 ± 0.59	1.88 ± 0.06	102.12 ± 8.95
		10.64	20.39 ± 0.37	2.21 ± 0.04	132.98 ± 11.43
600	4.50 ± 0.57	4.53	4.92 ± 0.29	1.09 ± 0.06	29.35 ± 1.52
		6.31	6.59 ± 0.18	1.46 ± 0.07	36.94 ± 2.82
		8.36	8.36 ± 0.32	1.86 ± 0.08	43.15 ± 2.63
		10.32	10.35 ± 0.58	2.20 ± 0.13	54.20 ± 3.26
800	1.98 ± 0.49	4.57	2.11 ± 0.28	1.07 ± 0.14	9.45 ± 0.99
		6.46	2.77 ± 0.22	1.40 ± 0.11	14.44 ± 1.53
		8.59	3.40 ± 0.19	1.71 ± 0.10	18.73 ± 1.72
		10.65	3.86 ± 0.14	1.95 ± 0.07	23.35 ± 2.36

Fig. 9 displays the stress-time curves of ECC within the strain rates of 10.32–10.95 s^{-1}, indicating that the elastic stage changed after exposure to different temperatures. At 20 and 105 °C, the specimens exhibited better bonding performance between PVA fibres and matrix, so the stress raised faster with loading time at the elastic stage. As PVA fibres melted at over 250 °C, the slope of the elastic stage dropped with the decrease of peak stress, and the variation of the stress-time curve was consistent with the change in failure pattern [59].
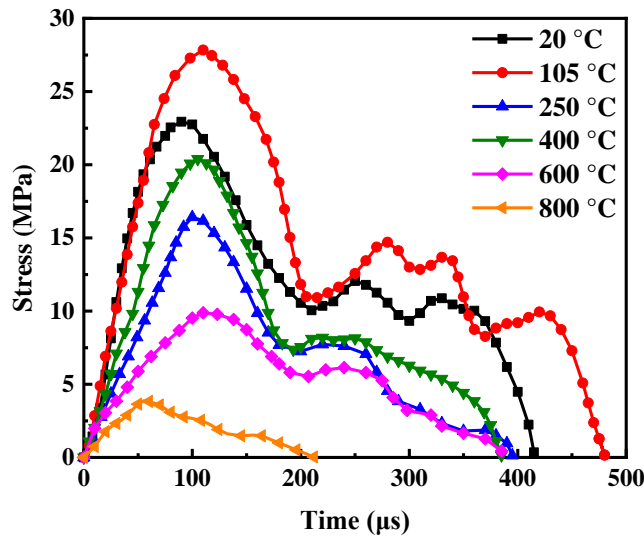

Fig. 9. Stress-time response of ECC after heating exposure at the strain rates of 10.32–10.95 s^{-1}.

3.4.2 Failure patterns

Cementitious composites including ECC are heterogeneous materials, so there exhibits a difference in the measured strain rate of ECC specimens under the same impact conditions [42,60]. In this study, the actual strain rate range was controlled around the target strain rate. Fig. 10 illustrates the failure patterns of all ECC specimens under impact loading. At 20 and 105 °C, the main crack passed through the centre of the specimen in the direction of the impact load and the whole specimen was split into two parts. With the increase of strain rate, the width of the central crack raised, while the ECC

specimen remained as one piece owing to the bridging effect of PVA fibre at lower strain rates. At higher strain rates (8.5–10.5 s^{-1}), the crush damage took place at the ends of the specimen in the form of triangle cracks and the area of the triangle enlarged with the increasing strain rate, which can be ascribed to the presence of initial cracks before the specimen reached the stress equilibrium state [42,61]. When the temperature exceeded 250 °C, the secondary cracks developed on the specimen surface due to the melting and vaporization of fibres under splitting the tensile load. Moreover, the width and number of secondary cracks raised significantly with the increase in temperature, and the failure mode of the specimen changed from tensile failure to tension-shear mixed failure. Under the strain rates of 10.32–10.95 s^{-1}, ECC specimens after treatment of 250–800 °C had a fragmentary failure during the dynamic splitting tensile process. Additionally, the size of fragments was reduced, and the number of fragments increased with the rising temperature. In general, the dynamic splitting tensile damage pattern of ECC became more severe with the rise of both exposure temperature and strain rate.
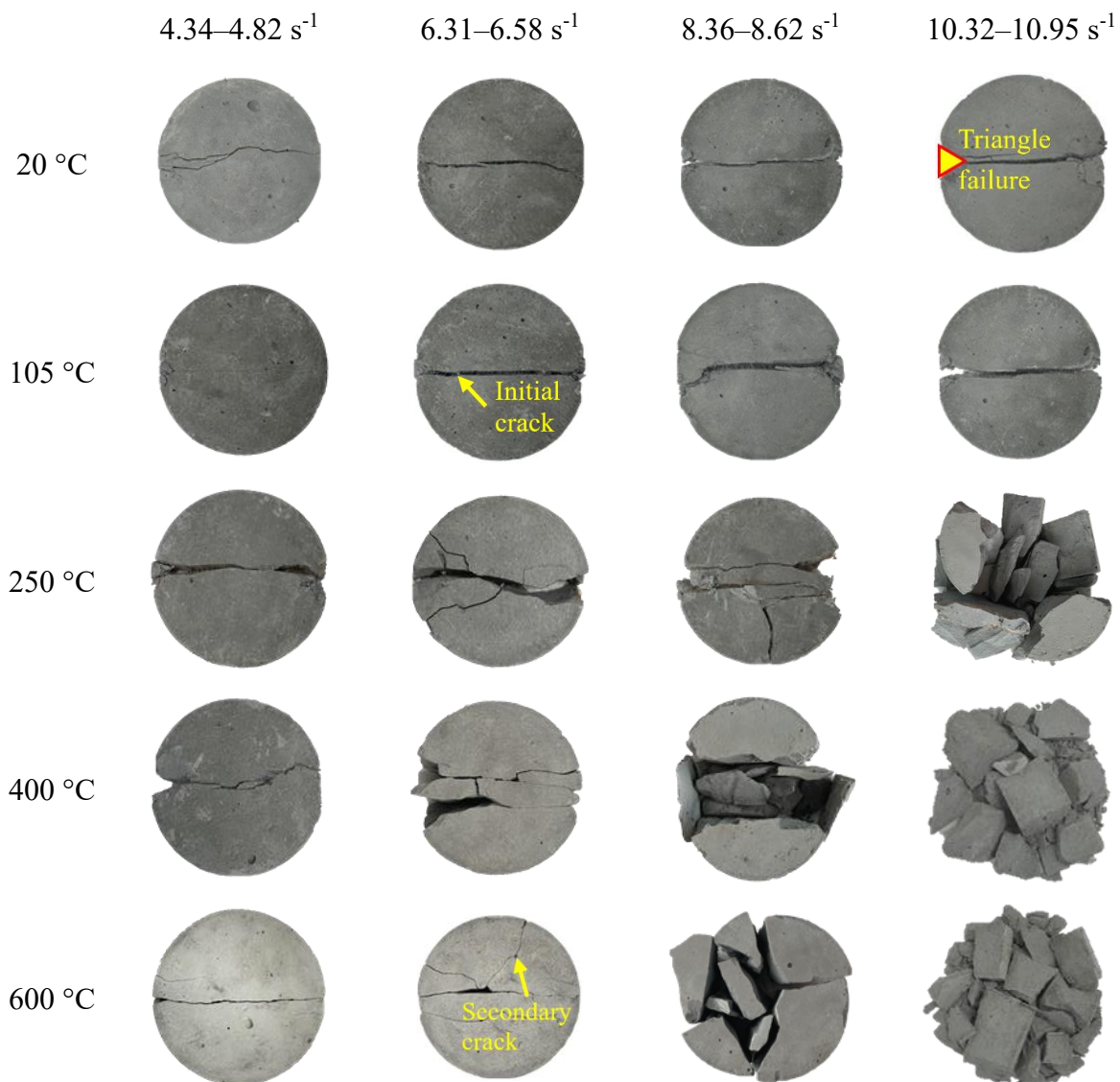
800 °C

Fig. 10. Failure patterns of ECC specimens under various strain rates.

3.4.3 Dynamic splitting tensile strength

Fig. 11 shows the variation of dynamic splitting tensile strength of ECC at strain rates of 4.34–10.95 s^{-1}. It can be seen that ECC specimens still exhibited a significant strain rate effect under dynamic load, regardless of exposure temperature, and the dynamic splitting tensile strength of specimens went up with the increase of strain rate, which can be ascribed to the complex physical and chemical changes at the microstructural level. With the increase in temperature, the variation in dynamic splitting tensile strength shows the same trend as the change in elastic modulus (Fig. 3) and static splitting tensile strength (Fig. 7). At 105°C, the dense structure and effective fibre bridging led to a rise in dynamic splitting strength by about 21.3–30.5% compared to that at 20 °C. As the temperature reached 250 °C, the specimens were rapidly damaged under dynamic loading. At 400 °C, the dynamic splitting tensile strength was greater than that at 250 °C, and accordingly the enhancement of dynamic splitting strength was greater than that of static splitting strength. At 600–800 °C, the dynamic splitting strength of the ECC varied less as the internal structure of the ECC matrix was loosened. Moreover, the decomposition of hydration products made ECC specimens unable to resist dynamic load and thus the dynamic splitting tensile properties were significantly reduced.
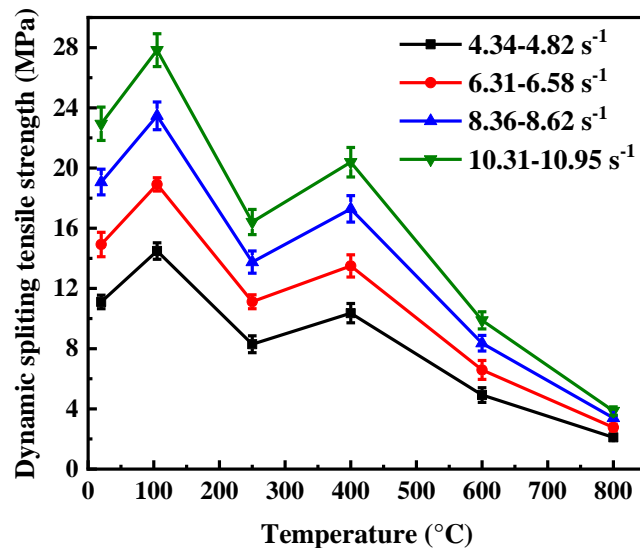

Fig. 11. Dynamic splitting tensile strength of ECC at elevated temperatures.

3.4.4 Dynamic increase factor

DIF has been widely applied to quantify the strength enhancement under impact loading [62]. The

DIF values were obtained by comparing the dynamic splitting tensile strength of ECC with the static splitting tensile strength (Table 4). Overall, DIF was improved by the strain rate effect but weakened by elevated temperature, as displayed in Fig. 12. The maximum DIF value exhibited at 105 °C, regardless of strain rate due to the enhanced bond between PVA fibre and matrix. As the temperature exceeded 250 °C, DIF at various strain rates dropped continuously with the increasing temperature. Specifically, DIF of ECC under strain rates of around 4.5, 6.5, 8.5 and 10.5 s^{-1} reduced by 10.8%, 13.6%, 17.4% and 21.7% at 800 °C relative to that at 20 °C, respectively. The thermally induced microcracks make the specimen easier to deform and intensify the impact damage degree of ECC under dynamic loading. In addition, the DIF growth rate by strain rate effect at an exposure temperature of under 250 °C was faster compared to that at the higher temperatures, indicating the strengthening effect of strain rate on ECC was pronounced before the melting of fibres.
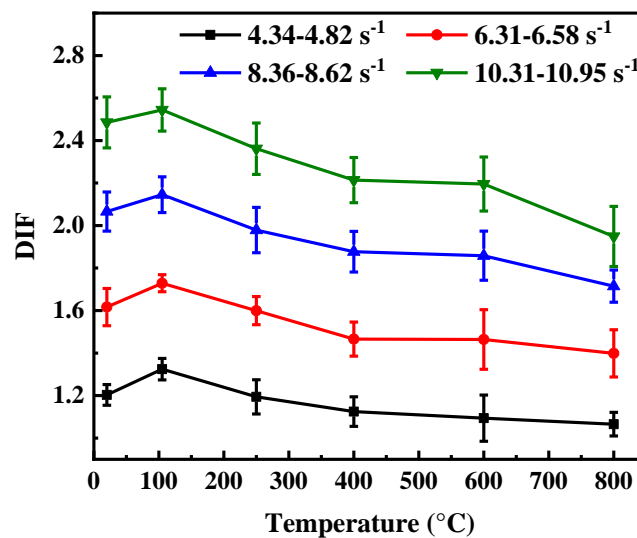

Fig. 12. DIF of ECC at elevated temperatures.

To better estimate the dynamic mechanical properties of ECC at various strain rates and elevated temperatures, an equation can be developed to describe the relationship between DIF and strain rate, which can be helpful for further structural design and theoretical analysis [63]. The relationship between DIF and logarithm of strain rate was fitted, as presented in Table 5. All correlation coefficients (R^2) of the fitted curves were greater than 0.98, suggesting the high reliability and validity of the proposed equations.

Table 5 Summary of the DIF equations.

Temperature (°C)	Fitted equation of DIF	R^2
20	DIF=3.195 log$\dot{\varepsilon}$ - 0.886	0.981
105	DIF=3.593 log$\dot{\varepsilon}$ - 1.165	0.993
250	DIF=3.265 log$\dot{\varepsilon}$ - 1.032	0.992
400	DIF=3.095 log$\dot{\varepsilon}$ - 0.996	0.993

| 600 | DIF=3.093 log$\dot{\varepsilon}$ - 0.970 | 0.990 |
| 800 | DIF=2.401 log$\dot{\varepsilon}$ - 0.527 | 0.998 |

3.4.5 Energy dissipation capacity

During the SHPB test, the incident strain $\varepsilon_i(t)$, reflection strain $\varepsilon_r(t)$ and transmission strain $\varepsilon_t(t)$ with time were measured by strain gauges attached to the incident and transmission bars. The dissipation energy $W_d(t)$ of ECC under SHPB can be obtained according to the energy balance of the incident energy $W_i(t)$, reflected energy $W_r(t)$ and transmitted energy $W_t(t)$ waves as follows [42]:

$$W_d(t) = W_i(t) - W_r(t) - W_t(t) \qquad (5)$$

$$W_i(t) = E_0 C_0 A_0 \int_0^t \varepsilon_i^2(t)\, \mathrm{d}t \qquad (6)$$

$$W_r(t) = E_0 C_0 A_0 \int_0^t \varepsilon_r^2(t)\, \mathrm{d}t \qquad (7)$$

$$W_t(t) = E_0 C_0 A_0 \int_0^t \varepsilon_t^2(t)\, \mathrm{d}t \qquad (8)$$

where C_0 is the longitudinal wave velocity in the steel bars (m/s).

The calculated dissipated energy data of ECC under impact loading is presented in Table 4, while Fig. 13 displays the dissipated energy of ECC at different strain rates with the increase of temperature, indicating the same change trend as shown in Fig. 11. At the strain rates of about 4.5, 6.5, 8.5, and 10.5 s^{-1}, the dissipated energy of ECC under dynamic splitting tensile load were 9.5–98.4, 14.4–136.2, 18.7–177.2, and 23.4–215.8 J, respectively. The variation in the number of cracks within the matrix at high strain rates was the main cause of the change in dissipated energy [42]. Under dynamic splitting loading, the fibre-matrix synergy, fibre debonding and fibre pull-out processes had additional effects on dissipated energy. With the increase of strain rate, the time for crack growth within the specimen was shorter and new cracks were produced directly. Thus, PVA fibres were pulled out, resulting in a significant rise in dissipated energy. Hence, the dissipated energy of ECC at 105 °C went up by 6.8–13.9% compared to that at 20 °C, which was reduced by 35.4–45.2% at 250 °C due to the phase change of PVA fibres. As the temperature reached 400 °C, the channels formed by the melting of fibres within the matrix were compacted during impact loading, leading to a 7.7–20.2% rise in dissipated energy of 400 °C compared to that at 250 °C. Within the temperature range of 400–800 °C, the internal structure of the specimen was damaged seriously, due to the evaporation of PVA fibres and decomposition of hydration products, reducing the bonding capacity of the matrix, as confirmed by the decrease of dissipated energy at elevated temperatures.
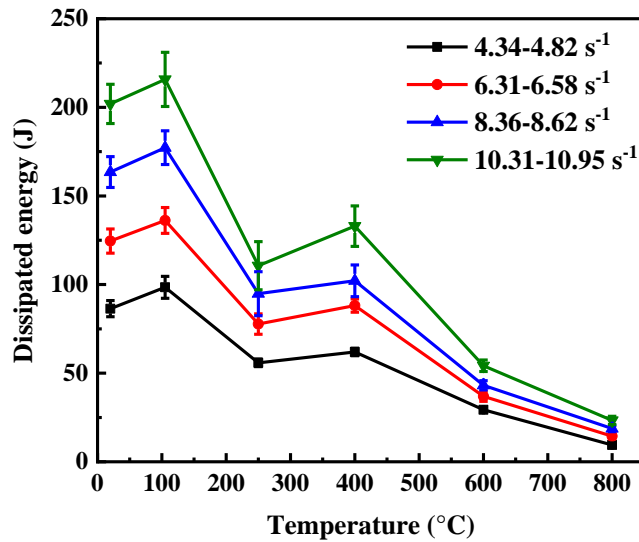
Fig. 13. Dissipated energy of ECC at elevated temperatures.

3.5 Pore pressure

Fig. 14 illustrates the pore pressure in ECC at different positions. Under unilateral heating, the pore pressure first went up and then dropped during heating. The peak value of pore pressure at 25 mm away from the heating surface reached 66.0 kPa, which was about 58.1% and 70.9% higher than those at 50 mm and 75 mm, respectively. Meanwhile, the temperature to reach the peak value of pore pressure slightly raised with the increase in distance between each position and the heating surface. As the free water evaporated, the vapour exerted pressure on the inner pore wall of ECC and the pore pressure increased with vapour content. Furthermore, ECC exhibited a stage of pore pressure accumulation before reaching the PVA fibre's melting point of 248 °C, which can be attributed to the blockage of vapour escape paths by fibre melt products. The microcracks were generated under the effect of pore pressure during the constant temperature process. With the rising temperature, the area of interfacial transition zone (ITZ) surrounding the fibres and porosity went up continuously. Thus, the vapour can escape through pores and cracks to release the pore pressure and reduce the risk of explosive spalling [64–66]. The pore pressure began to drop due to the increasing number of pores. Before 400 °C, the pore pressure caused by vapour had been almost completely released, which can be confirmed by the finding that the elastic modulus (Fig. 3) and splitting tensile strength (Figs. 7 and 11) of ECC at 400 °C would be slightly greater than that at 250 °C.
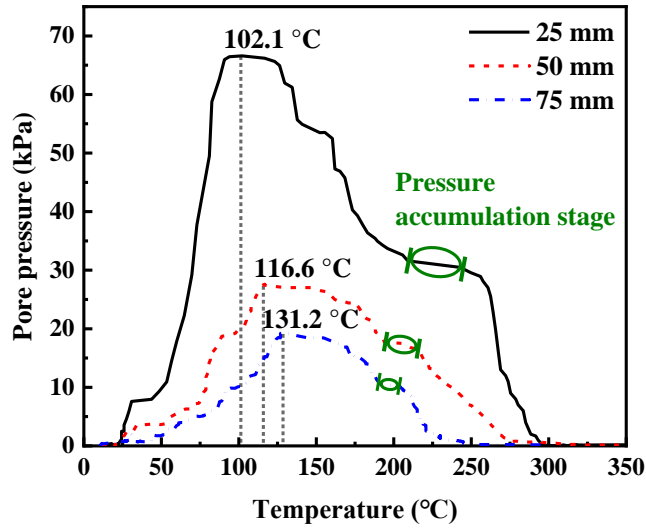
Fig. 14. Pore pressure of ECC specimen at various positions from the heating face.

3.6 Microstructure characteristics

3.6.1 Thermal analysis

Fig. 15 demonstrates the obtained TG and DSC curves of ECC samples. A decreasing trend of weight with the rising temperature can be shown in the TG curve, while the DSC curve suddenly decreased at 89.1, 438.8, and 718.3 °C, suggesting that the chemical changes at these temperatures. As discussed in Section 3.1, the weight loss of ECC can be ascribed to the evaporation of free and bound water as well as the decomposition of hydration products. This can be confirmed by the similar change for the TG curve and weight loss curve against temperature. When the temperature was 89.1 °C and 438.8 °C, the obvious endothermic phenomena can be ascribed to the decomposition of ettringite and cement hydrates including C-S-H and calcium hydroxide (CH) gels [44,67]. In addition, an exothermic peak can be observed at 718.3 °C, associated with the decomposition process of $CaCO_3$ in the calcite around this temperature range [68].
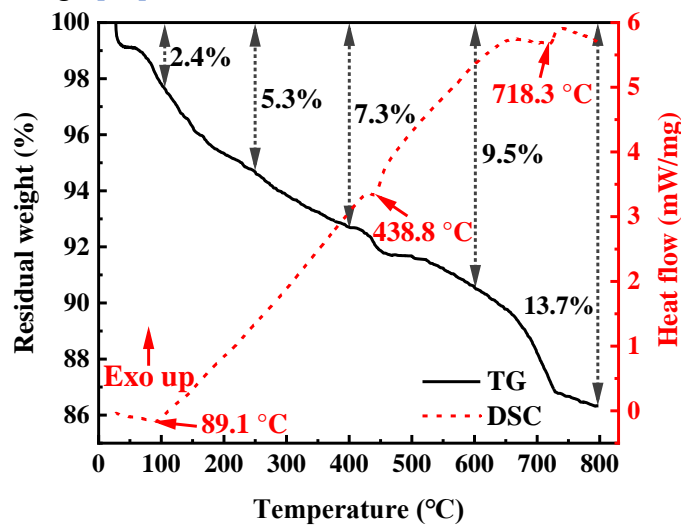

Fig. 15. Thermal analysis curves of ECC specimens.

3.6.2 Chemical composition

Fig. 16 illustrates the XRD spectra of ECC samples under different temperatures plotted from 10° to 80°. The samples contained a large amount of quartz sand and SiO_2 content that did not change during the heating process and no new substance was generated in the XRD spectra at 20, 105, and 250 °C. It can be explained that water was mainly evaporated in the samples from 20 to 400 °C with no chemical change observed in the samples and PVA fibres did not affect the chemical composition of ECC at these temperatures. At 400–600 °C, anhydrite and C_2S were generated from the dehydration of C-S-H gels and CH was decomposed into CaO and water. This process would absorb a certain amount of heating, as confirmed by the results of DSC. At 600–800 °C, most C-S-H gels decomposed and CO_2 was released, resulting in the weight loss and performance deterioration of ECC samples [21,69]. During this stage, the content of anhydrite increased with the presence of a new decomposition product (C_3A) in the matrix [69] and a large amount of C_2S was generated after ECC samples were heated to 800 °C, leading to the changes in internal microstructure of ECC [32]. The decomposition of cement hydrates was the main reason for the loss of mechanical properties of ECC.
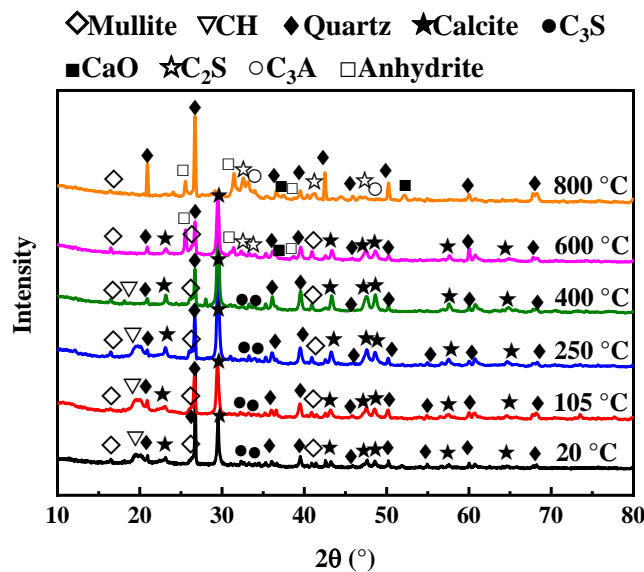

Fig. 16. XRD spectra of ECC specimens at elevated temperatures.

3.6.3 SEM observations

The SEM micrographs of fibre-matrix interfaces in the same ECC sample at different temperatures are shown in Fig. 17. At 20 °C, PVA fibres were well bonded to the mortar matrix (Fig. 17a). The difference in the thermal expansion coefficient of each component (e.g., cement hydrations, sand, and PVA fibre) led to the crack formation in the matrix during heating (Fig. 17b) [70]. When the temperature reached 250 °C, PVA fibre began to melt, leading to a wider fibre-matrix interface zone and the molten product adhered to the inner wall of pores. Moreover, as seen in Fig. 17c, the fibre

ends melt along with the formation of voids. Cracks were initially distributed near the contact surface between fibres and matrix due to the gained pore pressure, which grew and later got connected with the inherent defects. In addition, the pore pressure in ECC was effectively released due to the formation of pores by fibre melting, as discussed in Section 3.5.
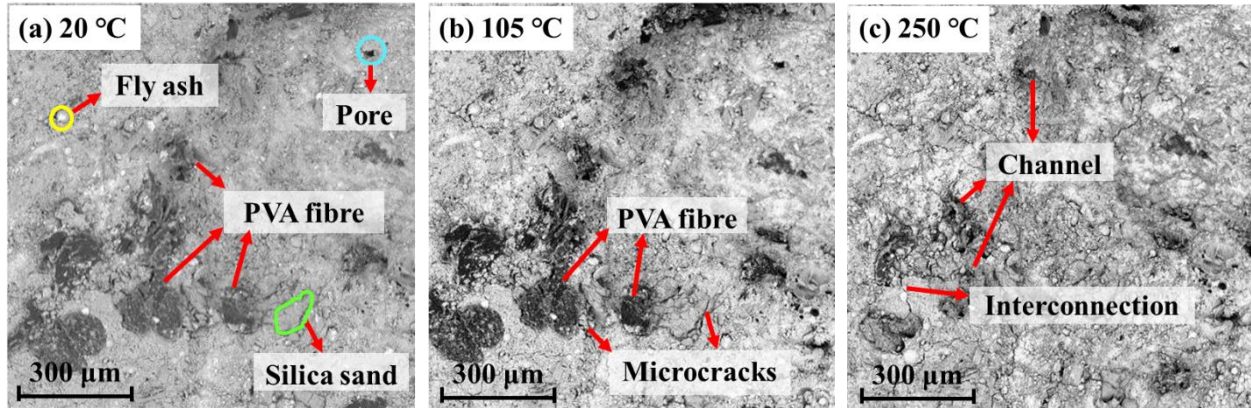

Fig. 17. Microstructural evolution of ECC specimen at elevated temperatures.

Fig. 18 shows the SEM images of PVA fibre morphology after the dynamic splitting tensile test and uniaxial tensile test. The friction effect between PVA fibre and matrix in the dynamic splitting tensile test mainly induced two failure modes: pull-out (Fig. 18a), and rupture (Fig. 18b). Fragments of ECC matrix can be observed on the surface of the pulled-out and ruptured fibres, indicating the great bonding role between PVA fibres and matrix. It is worth mentioning that the ruptured end of the fibre after dynamic fracture was smoother than the static uniaxial fracture end face (Fig. 18c), which is likely to be a major reason for the high dynamic dissipated energy.
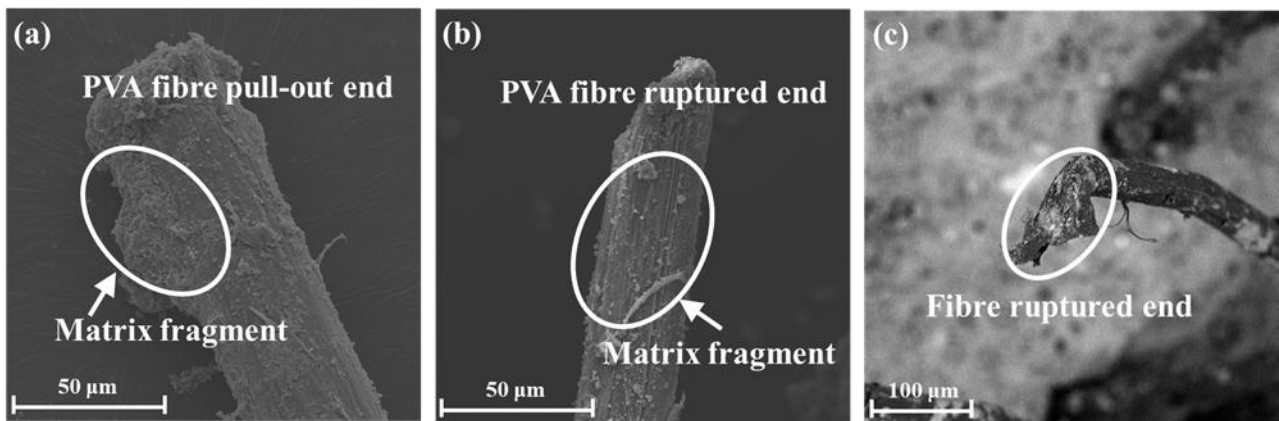

Fig. 18. SEM images of PVA fibre: (a) fibre pull-out end after dynamic test; (b) fibre ruptured end after dynamic test; (c) fibre rupture end after uniaxial tensile test.

3.6.4 Pore structure

Fig. 19 displays the pore size distribution of ECC samples exposed to elevated temperatures obtained from MIP tests. The pores in cementitious materials can be divided into five groups by diameter as per Refs. [27,71]: < 10 nm, 10–100 nm, 100–1000 nm, 1000–10000 nm, and > 10000 nm, which were

calculated and shown in Fig. 20. The porosity and average pore diameter of ECC at 20, 105, 250, 400, 600, and 800 °C was 18.4%, 20.2%, 16.9%, 21.3%, 25.9%, 37.8% and 31.3, 26.2, 19.8, 22.6, 39.7, 295.4 nm, respectively. After the exposure of 105 °C, the porosity of ECC went up by 1.8% compared to that at ambient temperature as the evaporation of partial free water inside the matrix increased the number of gel micro-pores. However, the average pore diameter dropped due to the further hydration of anhydrous cement and fly ash particles, resulting in the formation of more C-S-H gels in the ECC matrix [18,72].

Regarding the samples at 250 °C, the hydration degree of cement and fly ash particles increased, and the melted fibre residues filled part of the pores, resulting in a reduction in porosity. Thus, the paths for vapour release would be blocked and the internal microstructure of ECC would be damaged. Hence, more microcracks were generated in the weak surface and ITZ around the fibres [22], showing that the proportion of the pore (< 100 nm) content increased significantly. At 400 °C, the porosity raised by 2.9% compared to that at 20 °C and the pore size of 100–1000 nm content went up. Due to the expansion of the ITZ area around the pores induced by fibre melting and evaporation within the temperature range of 250–400 °C, as a result of which pores were formed at both ends of the melting fibres and the ITZ areas became wider. At this point, the vapour could quickly escape through the channels and thus the pore pressure would not induce a significant influence on the matrix. When the temperature exceeded 600 °C, the decomposition of C-S-H gels and CH would lead to an obvious rise in porosity [22,28]. The connections of microcracks and the collapse of the internal structure cause the increase of 1000–10000 nm pores [55]. Hence, the evolution of pore structure reflected the degradation of the matrix at elevated temperatures to a certain degree [21,73].
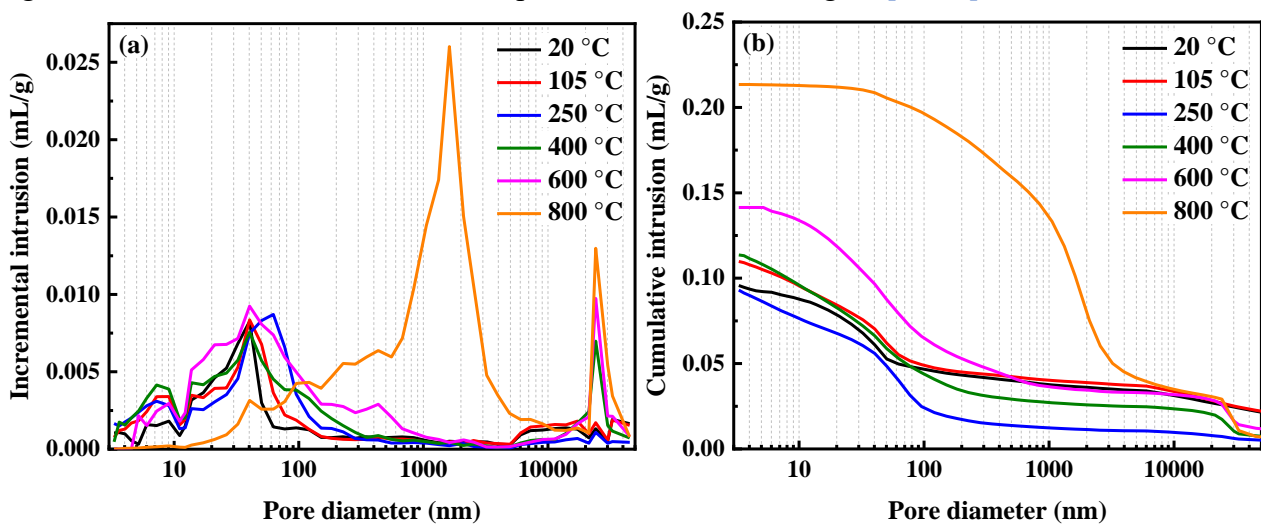

Fig. 19. Pore size distribution of ECC at elevated temperatures: (a) differential intruded pore volume; (b) cumulative intruded pore volume.
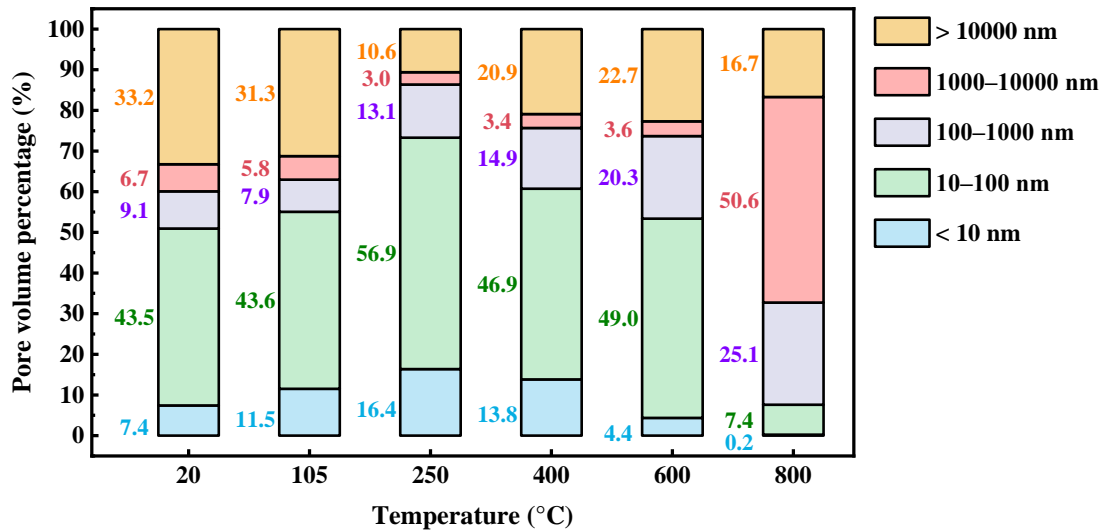
Fig. 20. Pore volume percentage of ECC at elevated temperatures.

4. Discussion

During the SHPB test, the stress concentration first appears at the position where the specimen contacts the steel bars, whilst the triangular failure zone on both sides of the specimen expands simultaneously with the rising strain rate. When the ECC specimen is subjected to impact loading, the initial crack expands from the centre to both sides along the loading direction, leading to the formation of the main crack along the central interface (Fig. 10). At the same time, the maximum internal stress of cylindrical ECC specimens occurs at the centre as per the fundamental theory of elasticity, and the compressive stress at this position is three times the tensile stress [74]. The compressive strength of concrete is about ten times the tensile strength, so it is judged that the tested specimen has a tensile failure [75]. At elevated temperatures, as illustrated in Fig. 21, the crack development of ECC took place with the increase of strain rate under two conditions, i.e., before and after the melting of PVA fibres, and accordingly the damage mechanism of ECC can be explained by the following two aspects.

(i) Before the melting of PVA fibres, the bonding between cement matrix and PVA fibre in ECC was enhanced after exposure to 105 °C than that at ambient temperature, as confirmed by the results of the uniaxial tensile test in Section 3.3.1. The dynamic splitting strength and dissipated energy of ECC at 105 °C raised by 21.3–30.5% and 6.8–13.9% compared to that at 20 °C, which can be attributed to the enhanced fibre-matrix bond under dynamic loading [1]. Besides, the dynamic splitting tensile properties of ECC specimens were also affected by the fibre-matrix interaction (i.e., fibre debonding, fibre pull-out and fibre rupture) and the development of microcracks. Under dynamic tensile loading, a rapid pull-out process consumed more energy before fibre failure and produced smoother fibre ends compared to that under static tensile loading. At lower strain rates (4.5–6.5 s⁻¹),

the PVA fibres at initial cracks were stretched and the specimen was damaged slightly (Fig. 21a and b). With the rising strain rate, the PVA fibres were deboned from the cement matrix and pulled out (Fig. 21c), resisting most of the impact loading and significantly raising the dynamic splitting behaviour [35]. At higher strain rates (8.5–10.5 s^{-1}), the width of initial crack was enlarged and the PVA fibres across macroscopic cracks were pulled out or ruptured under impact loading, as illustrated in Fig. 21d.

(ii) After the melting of PVA fibres, the cement matrix gradually lost the protection from bridging action of the PVA fibres and cracks rapidly developed under dynamic splitting tensile loading. As seen from the failure pattern, the number of secondary cracks increased along with the formation of primary cracks after the melting of PVA fibres (Fig. 21e). During this period, the external energy can only be absorbed by the crack propagation (Fig. 21f), and the number of cracks gradually went up with the increase of strain rate. When the exposure temperature exceeded 250 °C, the crack initiation points changed from the central maximum tensile point to multiple positions (Fig. 21g), attributed to the decomposition of cement hydrates and the raised porosity as confirmed by XRD and MIP results [76]. Moreover, ECC specimens exhibited rapid crack propagation at multiple positions after exposed to over 400 °C (Fig. 21h), and the failure mode changed from tensile damage to coupled tensile-shear damage. In addition, the further decomposition of cement hydrates at 400–800 °C significantly reduced the dynamic splitting properties of ECC, while the dynamic splitting strength and dissipated energy of ECC at 800 °C were only about 16.8–19.0% and 10.9–11.6% of that at 20 °C, respectively.
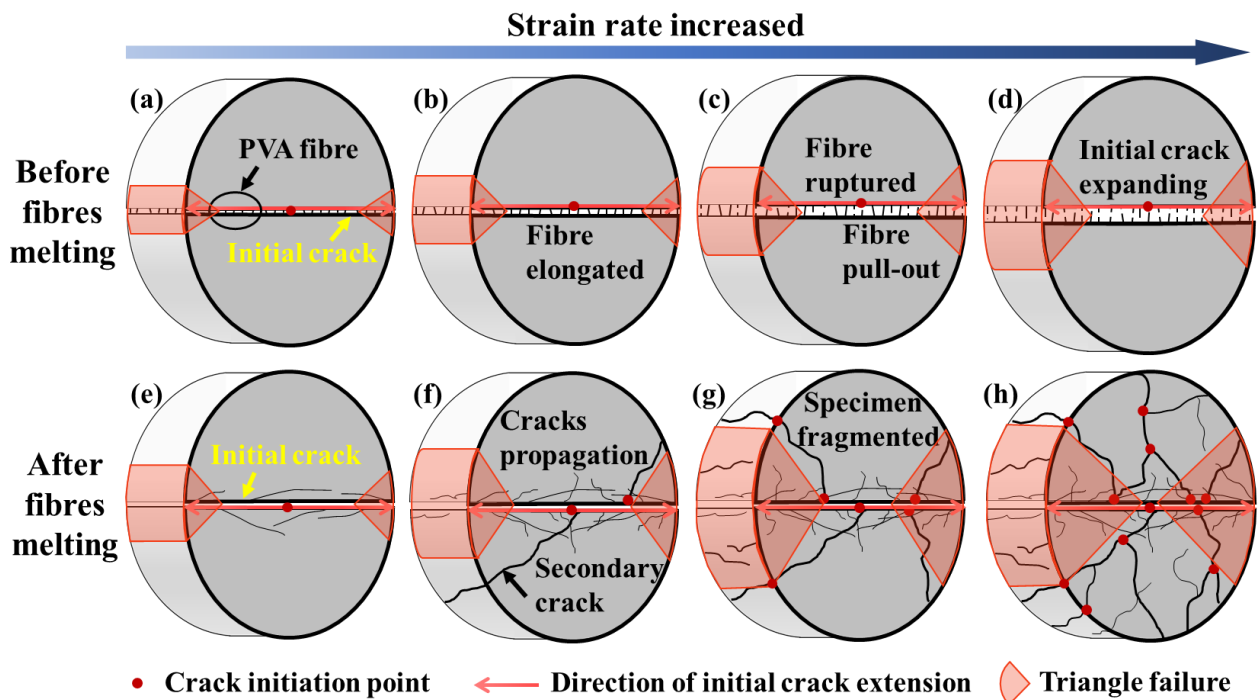

Fig. 21. A schematic illustration of crack development of ECC with the increasing strain rate.

5. Conclusions

In this study, a series of experiments were performed to explore the evolution of physical and static and dynamic splitting tensile properties as well as the microstructure of ECC after being subjected to elevated temperatures up to 800 °C. Based on the obtained experimental results, the main conclusions can be drawn as follows:

- Under dynamic tensile loading, ECC specimens were mainly split into two parts along the central crack, and crushing failure took place, followed by crack growth with the rising strain rate and exposure temperature. As the temperature increased to 250 °C, the damage degree of ECC was significantly raised, along with the reduction in particle size of the fragments.

- As the strain rate went up from 4.34 s^{-1} to 10.95 s^{-1}, the dynamic tensile properties in terms of dynamic splitting tensile strength, DIF and dissipated energy of ECC exhibited a rising trend regardless of elevated temperatures due to strain rate effect. The dynamic splitting strength and dissipated energy of ECC under the strain rate of around 10.5 s^{-1} were 0.66–1.07 and 0.98–1.47 times respectively higher than that at around 4.5 s^{-1} over the measured temperature range, which can be ascribed to the microcrack propagation and resistance of PVA fibres.

- With the increasing temperature, the dynamic tensile properties of ECC first increased and then declined up to 800 °C. At 105 °C, they reached the maximum values where the dynamic splitting strength and dissipated energy raised by 21.3–30.5% and 6.8–13.9% compared to that at 20 °C, respectively, attributed to the improved fibre-matrix interaction and denser microstructure of ECC matrix. Then, the reduction in dynamic tensile properties of ECC can be ascribed to the melting of PVA fibre, phase decomposition, and the development of microcracks. After being exposed to 800 °C, the residual dynamic splitting strength of ECC was only about 16.8–19.0%.

- Before the melting of PVA fibres, the pull-out and rupture of fibres greatly enhanced the dynamic tensile properties of ECC by resisting the growth of the central crack. When the temperature reached the melting point of PVA fibres, multiple microcracks were developed along with the central crack, due to the weakening of fibre-matrix interaction. In addition, the failure mode of ECC gradually transformed from tensile failure to coupled tensile-shear failure with the rising strain rate and elevated temperature.

References

[1]   Z.T. Chen, Y.Z. Yang, Y. Yan, Quasi-static and dynamic compressive mechanical properties of engineered cementitious composite incorporating ground granulated blast furnace slag, Mater. Des. 44 (2013) 500–508. https://doi.org/10.1016/j.matdes.2012.08.037.

[2]   X. Zhang, X. Wu, Y. Park, T. Zhang, X. Huang, F. Xiao, A. Usmani, Perspectives of big experimental database and artificial intelligence in tunnel fire research, Tunn. Undergr. Sp. Technol. 108 (2021) 103691. https://doi.org/10.1016/j.tust.2020.103691.

[3]   V.C. Li, Engineered Cementitious Composites (ECC) : Bendable Concrete for Sustainable and Resilient Infrastructure, Springer, 2019, Springer, 2019. https://doi.org/10.1007/978-3-662-58438-5.

[4]   K.Q. Yu, L.Z. Li, J.T. Yu, Y.C. Wang, J.H. Ye, Q.F. Xu, Direct tensile properties of engineered cementitious composites: A review, Constr. Build. Mater. 165 (2018) 346–362. https://doi.org/10.1016/j.conbuildmat.2017.12.124.

[5]   V.C. Li, Tailoring ECC for Special Attributes: A Review, Int. J. Concr. Struct. Mater. 6 (2012) 135–144. https://doi.org/10.1007/s40069-012-0018-8.

[6]   S.H. Said, H.A. Razak, The effect of synthetic polyethylene fiber on the strain hardening behavior of engineered cementitious composite (ECC), Mater. Des. 86 (2015) 447–457. https://doi.org/10.1016/j.matdes.2015.07.125.

[7]   V.C. Li, C. Wu, S.X. Wang, A. Ogawa, T. Saito, Interface tailoring for strain-hardening polyvinyl alcohol engineered cementitious composite (PVA-ECC), Aci Mater. J. 99 (2002) 463–472. https://doi.org/10.1016/S0042-207X(02)00187-2.

[8]   V.C. Li, M. Lepech, L. Lepech, Crack Resistant Concrete Material for Transportation Construction, Transp. Res. Board 83rd Annu. Meet. Washington, DC, CD Rom 04-4680. (2003) 4–4680.

[9]   J.C. Liu, K.H. Tan, D. Zhang, Multi-response optimization of post-fire performance of strain hardening cementitious composite, Cem. Concr. Compos. 80 (2017) 80–90. https://doi.org/10.1016/j.cemconcomp.2017.03.001.

[10]   Z. wei Cai, J. tao Yu, L. kang Tian, F. chi Liu, K. quan Yu, Fire resistance of post-earthquake steel beams insulated with a novel fire-resistive coating- FR-ECC, Eng. Struct. 246 (2021) 112887. https://doi.org/10.1016/j.engstruct.2021.112887.

[11]   D. Meng, C.K. Lee, Y.X. Zhang, Flexural and shear behaviours of plain and reinforced polyvinyl alcohol-engineered cementitious composite beams, Eng. Struct. 151 (2017) 261–272. https://doi.org/10.1016/j.engstruct.2017.08.036.

[12]   X.Y. Shang, J.T. Yu, L.Z. Li, Z.D. Lu, Shear strengthening of fire damaged RC beams with stirrup reinforced engineered cementitious composites, Eng. Struct. 210 (2020) 110263.

https://doi.org/10.1016/j.engstruct.2020.110263.

[13] M. Maalej, S.T. Quek, S.F.U. Ahmed, J. Zhang, V.W.J. Lin, K.S. Leong, Review of potential structural applications of hybrid fiber Engineered Cementitious Composites, Constr. Build. Mater. 36 (2012) 216–227. https://doi.org/10.1016/j.conbuildmat.2012.04.010.

[14] B. Gencturk, A.S. Elnashai, M.D. Lepech, S. Billington, Behavior of Concrete and ECC Structures under Simulated Earthquake Motion, J. Struct. Eng. 139 (2013) 389–399. https://doi.org/10.1061/(Asce)St.1943-541x.0000667.

[15] Q. Wang, B.Y. Yao, R.Z. Lu, Behavior Deterioration and Microstructure Change of Polyvinyl Alcohol Fiber-Reinforced Cementitious Composite (PVA-ECC) after Exposure to Elevated Temperatures, Materials (Basel). 13 (2020) 5539. https://doi.org/10.3390/ma13235539.

[16] X. Li, Y. Li, M. Yan, W. Meng, X. Lu, K. Chen, Y. Bao, Cyclic behavior of joints assembled using prefabricated beams and columns with Engineered Cementitious Composite (ECC), Eng. Struct. 247 (2021). https://doi.org/10.1016/j.engstruct.2021.113115.

[17] D. Gu, J. Pan, S. Mustafa, Y. Huang, M. Luković, Shear transfer mechanism in reinforced engineered cementitious composite (ECC) beams: Quantification of Vs and Vc, Eng. Struct. 261 (2022). https://doi.org/10.1016/j.engstruct.2022.114282.

[18] Z.G. Zhang, J.C. Liu, X.Q. Xu, L.Q. Yuan, Effect of sub-elevated temperature on mechanical properties of ECC with different fly ash contents, Constr. Build. Mater. 262 (2020) 120096. https://doi.org/10.1016/j.conbuildmat.2020.120096.

[19] X. Li, Y. Bao, L. Wu, Q. Yan, H. Ma, G. Chen, H. Zhang, Thermal and mechanical properties of high-performance fiber-reinforced cementitious composites after exposure to high temperatures, Constr. Build. Mater. 157 (2017) 829–838. https://doi.org/10.1016/j.conbuildmat.2017.09.125.

[20] P.S. Bhat, V. Chang, M. Li, Effect of elevated temperature on strain-hardening engineered cementitious composites, Constr. Build. Mater. 69 (2014) 370–380. https://doi.org/10.1016/j.conbuildmat.2014.07.052.

[21] T.K. Erdem, Specimen size effect on the residual properties of engineered cementitious composites subjected to high temperatures, Cem. Concr. Compos. 45 (2014) 1–8. https://doi.org/10.1016/j.cemconcomp.2013.09.019.

[22] M. Sahmaran, M. Lachemi, V.C. Li, Assessing Mechanical Properties and Microstructure of Fire-Damaged Engineered Cementitious Composites, Aci Mater. J. 107 (2010) 297–304. https://doi.org/10.14359/51663759.

[23] C.S. Poon, Z.H. Shui, L. Lam, Compressive behavior of fiber reinforced high-performance concrete subjected to elevated temperatures, Cem. Concr. Res. 34 (2004) 2215–2222. https://doi.org/10.1016/j.cemconres.2004.02.011.

[24] W. Zheng, B. Luo, Y. Wang, Stress–strain relationship of steel-fibre reinforced reactive powder concrete at elevated temperatures, Mater. Struct. Constr. 48 (2015) 2299–2314. https://doi.org/10.1617/s11527-014-0312-9.

[25] Q. Du, J. Wei, J. Lv, Effects of High Temperature on Mechanical Properties of Polyvinyl Alcohol Engineered Cementitious Composites (PVA-ECC), Int. J. Civ. Eng. 16 (2018) 965–972. https://doi.org/10.1007/s40999-017-0245-0.

[26] V. Mechtcherine, F.D. Silva, S. Muller, P. Jun, R.D. Toledo, Coupled strain rate and temperature effects on the tensile behavior of strain-hardening cement-based composites (SHCC) with PVA fibers, Cem. Concr. Res. 42 (2012) 1417–1427. https://doi.org/10.1016/j.cemconres.2012.08.011.

[27] J.J. Luo, Z.W. Cai, K.Q. Yu, W.J. Zhu, Z.D. Lu, Temperature impact on the micro-structures and mechanical properties of high-strength engineered cementitious composites, Constr. Build. Mater. 226 (2019) 686–698. https://doi.org/10.1016/j.conbuildmat.2019.07.322.

[28] M. Sahmaran, E. Ozbay, H.E. Yucel, M. Lachemi, V.C. Li, Effect of Fly Ash and PVA Fiber on Microstructural Damage and Residual Properties of Engineered Cementitious Composites Exposed to High Temperatures, J. Mater. Civ. Eng. 23 (2011) 1735–1745. https://doi.org/10.1061/(asce)mt.1943-5533.0000335.

[29] M.D. Magalhaes, R.D. Toledo, E.D.R. Fairbairn, Thermal stability of PVA fiber strain hardening cement-based composites, Constr. Build. Mater. 94 (2015) 437–447. https://doi.org/10.1016/j.conbuildmat.2015.07.039.

[30] J.C. Liu, K.H. Tan, Fire resistance of strain hardening cementitious composite with hybrid PVA and steel fibers, Constr. Build. Mater. 135 (2017) 600–611. https://doi.org/10.1016/j.conbuildmat.2016.12.204.

[31] K.Q. Yu, J.G. Dai, Z.D. Lu, C.K.Y. Leung, Mechanical Properties of Engineered Cementitious Composites Subjected to Elevated Temperatures, J. Mater. Civ. Eng. 27 (2014) 4014268. https://doi.org/10.1061/(Asce)Mt.1943-5533.0001241.

[32] J.C. Liu, K.H. Tan, S.X. Fan, Residual mechanical properties and spalling resistance of strain-hardening cementitious composite with Class C fly ash, Constr. Build. Mater. 181 (2018) 253–265. https://doi.org/10.1016/j.conbuildmat.2018.06.009.

[33] M.F. Kai, Y. Xiao, X.L. Shuai, G. Ye, Compressive Behavior of Engineered Cementitious Composites under High Strain-Rate Loading, J. Mater. Civ. Eng. 29 (2017) 1–8. https://doi.org/10.1061/(asce)mt.1943-5533.0001781.

[34] K.H. Tan, E.H. Yang, S.B. Kang, T.Y. Wahyudi, Mechanical Behaviour of Engineered Cementitious Composites under Quasi-Static and High Strain Rate Applications, Adv. Mater. Res. 1129 (2015) 10–18. https://doi.org/10.4028/www.scientific.net/amr.1129.10.

[35] A.A. Heravi, I. Curosu, V. Mechtcherine, A gravity-driven split Hopkinson tension bar for

investigating quasi-ductile and strain-hardening cement-based composites under tensile impact loading, Cem. Concr. Compos. 105 (2020) 103430. https://doi.org/10.1016/j.cemconcomp.2019.103430.

[36] V. Mechtcherine, F. De Andrade Silva, M. Butler, D. Zhu, B. Mobasher, S.L. Gao, E. M̈der, Behaviour of strain-hardening cement-based composites under high strain rates, J. Adv. Concr. Technol. 9 (2011) 51–62. https://doi.org/10.3151/jact.9.51.

[37] V. Mechtcherine, O. Millon, M. Butler, K. Thoma, Mechanical behaviour of strain hardening cement-based composites under impact loading, Cem. Concr. Compos. 33 (2011) 1–11. https://doi.org/10.1016/j.cemconcomp.2010.09.018.

[38] I. Curosu, V. Mechtcherine, D. Forni, E. Cadoni, Performance of various strain-hardening cement-based composites (SHCC) subject to uniaxial impact tensile loading, Cem. Concr. Res. 102 (2017) 16–28. https://doi.org/10.1016/j.cemconres.2017.08.008.

[39] ASTM E831-19, Standard Test Method for Linear Thermal Expansion of Solid Materials by Thermomechanical Analysis, ASTM International, West Conshohocken, PA, 2019 (n.d.), www.astm.org, n.d.

[40] ASTM C469, Standard test method for static modulus of elasticity and Poisson's ratio of concrete in compression, ASTM International, West Conshohocken, PA, United States, 2014, n.d.

[41] Japan Society of Civil Engineers, Recommendations for Design and Construction of High Performance Fiber Reinforced Cement Composites with Multiple Fine Cracks (HPFRCC), Concrete Engineering Series No, 2008, p. 82, n.d.

[42] M. Chen, H. Zhong, H. Wang, M.Z. Zhang, Behaviour of recycled tyre polymer fibre reinforced concrete under dynamic splitting tension, Cem. Concr. Compos. 114 (2020) 103764. https://doi.org/10.1016/j.cemconcomp.2020.103764.

[43] C.M. Lewandowski, N. Coinvestigator, C.M. Lewandowski, Split Hopkinson (Kolsky) Bar: Design, Testing and Applications, Springer US, 2015.

[44] M. Chen, Z.H. Sun, W.L. Tu, X. Yan, M.Z. Zhang, Behaviour of recycled tyre polymer fibre reinforced concrete at elevated temperatures, Cem. Concr. Compos. 124 (2021) 104257. https://doi.org/10.1016/j.cemconcomp.2021.104257.

[45] P. Kalifa, F.-D. Menneteau, D. Quenard, Spalling and pore pressure in HPC at high temperatures, Cem. Concr. Res. 30 (2000) 1915–1927. https://doi.org/10.1016/S0008-8846(00)00384-7.

[46] A.A. Deshpande, D. Kumar, R. Ranade, Influence of high temperatures on the residual mechanical properties of a hybrid fiber-reinforced strain-hardening cementitious composite, Constr. Build. Mater. 208 (2019) 283–295. https://doi.org/10.1016/j.conbuildmat.2019.02.129.

[47]   S. Rawat, C.K. Lee, Y.X. Zhang, Performance of fibre-reinforced cementitious composites at elevated temperatures: A review, Constr. Build. Mater. 292 (2021) 123382. https://doi.org/10.1016/j.conbuildmat.2021.123382.

[48]   D. Zhang, J. Yu, H.L. Wu, B. Jaworska, B.R. Ellis, V.C. Li, Discontinuous micro-fibers as intrinsic reinforcement for ductile Engineered Cementitious Composites (ECC), Compos. B Eng. 184 (2020) 107741. https://doi.org/10.1016/j.compositesb.2020.107741.

[49]   S. Sanchayan, S.J. Foster, High temperature behaviour of hybrid steel–PVA fibre reinforced reactive powder concrete, Mater. Struct. 49 (2016) 769–782. https://doi.org/10.1617/s11527-015-0537-2.

[50]   M. Said, A.A. Abd El-Azim, M.M. Ali, H. El-Ghazaly, I. Shaaban, Effect of elevated temperature on axially and eccentrically loaded columns containing Polyvinyl Alcohol (PVA) fibers, Eng. Struct. 204 (2020) 110065. https://doi.org/10.1016/j.engstruct.2019.110065.

[51]   Q. Zhang, V.C. Li, Development of durable spray-applied fire-resistive Engineered Cementitious Composites (SFR-ECC), Cem. Concr. Compos. 60 (2015) 10–16. https://doi.org/10.1016/j.cemconcomp.2015.03.012.

[52]   J. Zhou, S.Z. Qian, G. Ye, O. Copuroglu, K. van Breugel, V.C. Li, Improved fiber distribution and mechanical properties of engineered cementitious composites by adjusting the mixing sequence, Cem. Concr. Compos. 34 (2012) 342–348. https://doi.org/10.1016/j.cemconcomp.2011.11.019.

[53]   H. Zhong, M.Z. Zhang, Effect of recycled tyre polymer fibre on engineering properties of sustainable strain hardening geopolymer composites, Cem. Concr. Compos. 122 (2021) 104167. https://doi.org/10.1016/j.cemconcomp.2021.104167.

[54]   K.Q. Yu, Y. Ding, Y.X. Zhang, Size effects on tensile properties and compressive strength of engineered cementitious composites, Cem. Concr. Compos. 113 (2020) 103691. https://doi.org/10.1016/j.cemconcomp.2020.103691.

[55]   C.L. Chan, M. Zhang, Behaviour of strain hardening geopolymer composites at elevated temperatures, Cem. Concr. Compos. 132 (2022) 104634. https://doi.org/10.1016/j.cemconcomp.2022.104634.

[56]   H.L. Wu, D. Zhang, B.R. Ellis, V.C. Li, Mechanical behavior of carbonated MgO-based Engineered Cementitious Composite (ECC) after high temperatures exposure, Cem. Concr. Compos. 124 (2021) 104255. https://doi.org/10.1016/j.cemconcomp.2021.104255.

[57]   J.T. Yu, J.H. Lin, Z.G. Zhang, V.C. Li, Mechanical performance of ECC with high-volume fly ash after sub-elevated temperatures, Constr. Build. Mater. 99 (2015) 82–89. https://doi.org/10.1016/j.conbuildmat.2015.09.002.

[58]   Z.G. Zhang, S.Z. Qian, H. Ma, Investigating mechanical properties and self-healing behavior

of micro-cracked ECC with different volume of fly ash, Constr. Build. Mater. 52 (2014) 17–23. https://doi.org/10.1016/j.conbuildmat.2013.11.001.

[59] X. Zhao, S.L. Xu, Q.H. Li, B.K. Chen, Coupled effects of high temperature and strain rate on compressive properties of hybrid fiber UHTCC, Mater. Struct. 52 (2019). https://doi.org/10.1617/s11527-019-1391-4.

[60] M. Chen, W. Chen, H. Zhong, D. Chi, Y.H. Wang, M.Z. Zhang, Experimental study on dynamic compressive behaviour of recycled tyre polymer fibre reinforced concrete, Cem. Concr. Compos. 98 (2019) 95–112. https://doi.org/10.1016/j.cemconcomp.2019.02.003.

[61] X.D. Chen, L.M. Ge, J.K. Zhou, S.X. Wu, Dynamic Brazilian test of concrete using split Hopkinson pressure bar, Mater. Struct. 50 (2017) 1. https://doi.org/10.1617/s11527-016-0885-6.

[62] J. Xiao, L. Li, L. Shen, C.S. Poon, Compressive behaviour of recycled aggregate concrete under impact loading, Cem. Concr. Resea. 71 (2015) 46–55. https://doi.org/10.1016/j.cemconres.2015.01.014.

[63] H. Su, J. Xu, W. Ren, Mechanical properties of geopolymer concrete exposed to dynamic compression under elevated temperatures, Ceram. Int. 42 (2016). https://doi.org/10.1016/j.ceramint.2015.11.055.

[64] A. Bilodeau, V.K.R. Kodur, G.C. Hoff, Optimization of the type and amount of polypropylene fibres for preventing the spalling of lightweight concrete subjected to hydrocarbon fire, Cem. Concr. Compos. 26 (2004) 163–174. https://doi.org/10.1016/S0958-9465(03)00085-4.

[65] J. Xiao, H. Falkner, On residual strength of high-performance concrete with and without polypropylene fibres at elevated temperatures, Fire Saf. J. 41 (2006) 115–121. https://doi.org/10.1016/j.firesaf.2005.11.004.

[66] Y. Li, K.H. Tan, E.-H. Yang, Synergistic effects of hybrid polypropylene and steel fibers on explosive spalling prevention of ultra-high performance concrete at elevated temperature, Cem. Concr. Compos. 96 (2019) 174–181. https://doi.org/10.1016/j.cemconcomp.2018.11.009.

[67] A. Noumowe, Mechanical properties and microstructure of high strength concrete containing polypropylene fibres exposed to temperatures up to 200 °c, Cem. Concr. Res. 35 (2005). https://doi.org/10.1016/j.cemconres.2005.03.007.

[68] D. Zhang, B. Jaworska, H. Zhu, K. Dahlquist, V.C. Li, Engineered Cementitious Composites (ECC) with limestone calcined clay cement (LC3), Cem. Concr. Compos. 114 (2020) 103766. https://doi.org/10.1016/j.cemconcomp.2020.103766.

[69] G.F. Peng, Z.S. Huang, Change in microstructure of hardened cement paste subjected to elevated temperatures, Constr. Build. Mater. 22 (2008) 593–599.

https://doi.org/10.1016/j.conbuildmat.2006.11.002.

[70] D. Zhang, A. Dasari, K.H. Tan, On the mechanism of prevention of explosive spalling in ultra-high performance concrete with polymer fibers, Cem. Concr. Res. 113 (2018) 169–177. https://doi.org/10.1016/j.cemconres.2018.08.012.

[71] T. Zhang, Y. Zhang, H. Zhu, Z. Yan, Characterizing the thermal properties of hybrid polypropylene-steel fiber reinforced concrete under heat exposure : Insights into fiber geometry and orientation distribution, Compos. Struct. 275 (2021) 114457. https://doi.org/10.1016/j.compstruct.2021.114457.

[72] G.A. Khoury, Compressive strength of concrete at high temperatures: a reassessment, Mag. Concr. Res. 44 (161) (1992) 291-309, https://doi.org/10.1680/macr.1992.44.161.291, n.d. https://doi.org/10.1680/macr.1992.44.161.291.

[73] Y.N. Chan, X. Luo, W. Sun, Compressive strength and pore structure of high-performance concrete after exposure to high temperature up to 800°C, Cem. Concr. Resea. 30 (2000) 247–251. https://doi.org/10.1016/S0008-8846(99)00240-9.

[74] N.I. Muschelišvilli, Some basic problems of the mathematical theory of elasticity: fundamental equations, plane theory of elasticity, torsion, and bending, P.Noordhoff Ltd, 1963., n.d.

[75] M. Chen, H. Si, X. Fan, Y. Xuan, M. Zhang, Dynamic compressive behaviour of recycled tyre steel fibre reinforced concrete, Constr. Build. Mater. 316 (2022) 125896. https://doi.org/10.1016/j.conbuildmat.2021.125896.

[76] T. Zhang, M. Zhang, Y. Shen, H. Zhu, Z. Yan, Mitigating the damage of ultra-high performance concrete at elevated temperatures using synergistic flame-retardant polymer fibres, Cem. Concr. Res. 158 (2022) 106835. https://doi.org/10.1016/J.CEMCONRES.2022.106835.